

# A $V_{S30}$ Map for New Zealand Based on Geologic and Terrain Proxy Variables and Field Measurements

Kevin M. Foster,<sup>a)</sup> M.EERI, Brendon A. Bradley,<sup>a)</sup> M.EERI,  
Christopher R. McGann,<sup>a)</sup> and Liam M. Wotherspoon,<sup>b)</sup> M.EERI

A time-averaged 30-m-depth shear wave velocity ( $V_{S30}$ ) map is developed for New Zealand as a weighted combination of a geology-based and a terrain-based model. A Bayesian updating process allows local  $V_{S30}$  measurements to control model estimates where data exist and uses model estimates developed for other parts of the world where local data are sparse or nonexistent. Geostatistical interpolation is performed on the geology-based and terrain-based models using local  $V_{S30}$  measurements to constrain the model in the vicinity of data. Conventional regression kriging is compared with a flexible multivariate normal (MVN) approach that allows for arbitrary assumptions regarding measurement uncertainty at each data location. A modification to the covariance structure in the MVN application allows for more realistic estimates by reducing undesirable extrapolation across geologic boundaries. The results of kriging and MVN approaches are compared. The geology-based and terrain-based MVN models are combined to produce a final model suitable for engineering applications. The 100-m resolution map outputs are publicly available. [DOI: 10.1193/121118EQS281M]

## INTRODUCTION

$V_{S30}$ , the time-averaged vertical shear wave velocity in the uppermost 30 m, is widely used in earthquake engineering research and practice. Owing to the expense and difficulty of measuring  $V_{S30}$  directly, recent work has been devoted to developing  $V_{S30}$  models using  $V_{S30}$ -correlated proxy data. The work presented herein represents an attempt to incorporate the best recent practices for modeling  $V_{S30}$  (e.g., [Yong et al. 2012](#), [Thompson et al. 2014](#), [Parker et al. 2017](#), [Ahdi et al. 2017b](#)) using both available proxy data and direct  $V_{S30}$  measurements (with arbitrarily specified measurement uncertainty) within a statistical framework that treats uncertainty as an essential model component and allows consistent incremental improvements as new  $V_{S30}$  data are collected.

Others have applied methods similar to those presented here for mapping  $V_{S30}$  by proxy methods, where continuous and readily available proxy data are correlated with  $V_{S30}$  measurements and used to estimate  $V_{S30}$  in regions where direct measurements have not been taken. Generally, the proxy data include geology and topographic data. First, studies from

---

<sup>a)</sup> Department of Civil and Natural Resources Engineering, University of Canterbury, Christchurch, New Zealand; Email: kevin.foster@pg.canterbury.ac.nz (K. M. F.)

<sup>b)</sup> Civil and Environmental Engineering, University of Auckland, Auckland, New Zealand

around the world are summarized, and then prior work in New Zealand (NZ) is highlighted, with a focus on the additional contributions to be presented in the work herein.

Wills and Clahan (2006) developed a  $V_{S30}$  map for California based on surface geology. Geology-based  $V_{S30}$  mapping is confounded by the fact that mapped geologic units are frequently less than 30 m thick. Wills and Clahan (2006) handled this problem for alluvial basins by assigning locations in California to “shallow” or “deep” basin categories on the basis of areal extent: narrow valleys and locations near the base of steep mountains were assigned “shallow” categories, whereas extensive basins were assigned “deep” status. Wills and Clahan (2006) also separated alluvial units into fine, coarse, and mixed/undifferentiated bins for better  $V_{S30}$  discrimination. Wills and Gutierrez (2009) introduced a slope-dependent component to  $V_{S30}$  modeling. Topographic slope is slightly correlated with  $V_{S30}$ , at least for soil deposits, because of the depositional characteristics. For example, the size of particles dropping out of suspension in an alluvial depositional environment is correlated with flow velocity and, in turn, the slope of the landscape. The range and complexity of surficial rock depositional mechanisms renders this correlation virtually nonexistent for rock.

Building on the Wills and Clahan (2006) study, Thompson et al. (2014) developed a regional  $V_{S30}$  map for California that added topographic slope-based modifications (Wills and Gutierrez 2009, Allen and Wald 2007) to soil categories. Additionally, the well-known regression kriging (RK) approach was applied to the mapping, bringing model predictions into agreement with measurements locally. The kriging uncertainty in this study can be evaluated alongside the model predictions for a first-order, low-end assessment of expected disparity between model and reality. Importantly, kriging uncertainty is entirely a product of measurement locations and “globally” derived variogram, meaning that the mapped uncertainty is not conditioned on individual geology-based polygons.

Lee and Tsai (2008) generated a  $V_{S30}$  map of Taiwan in a two-step process, first generating a correlation-based model for  $V_{S30}$  using standard penetration testing (SPT) blow counts, then applying this model to a larger data set. The resulting model was kriged. Wald et al. (2011) proposed a generalized framework for  $V_{S30}$  mapping, recommending a hierarchal model with a topographic slope (being globally available) as the primary proxy variable and generating individual linear slope- $V_{S30}$  relations for significant geology categories. They demonstrated the method by producing a map of Taiwan and employing kriging to honor local observations.

Vilanova et al. (2018) developed a  $V_{S30}$  map for Portugal based on geology. Statistical testing was performed on candidate geologic units to optimize discrimination. Spatial declustering methods were evaluated but found to have non-negligible impact in only one of six candidate geologic units. After eliminating nondiscriminating categories, only three distinct geologic categories were used in the final model.

Ahdi et al. developed geology-based and topography-based  $V_{S30}$  models for Alaska (Ahdi et al. 2017b) and the Pacific Northwest (Ahdi et al. 2017a). The methods employed were similar to Thompson et al. (2014), although Ahdi et al. did not incorporate any geostatistical methods. Ahdi et al. reevaluated the geologic classification process, and hence the final product employs geologic categories that are distinct and generally more discriminating than the Thompson et al. (2014) categories. Parker et al. (2017) developed  $V_{S30}$  estimates for Central

and Eastern North America based on geology, topographic slope, and indicator variables to indicate significant sedimentary basins and the extent of Wisconsin glaciation. Basins and past glaciation were noted as having a strong correlation with observed  $V_{S30}$  values.

Yong et al. (2012) applied an automated digital elevation model (DEM)-based 16-category terrain classification scheme (Iwahashi and Pike 2007) to the problem of  $V_{S30}$  modeling. The terrain classification technique divides a map domain into bins based on slope, then further subdivides each bin into categories on the basis of local convexity and a local roughness measure. The results were used to generate worldwide  $V_{S30}$  maps. A later comprehensive review of proxy-based  $V_{S30}$  measurements (Yong 2016) examined the performance of this technique using newly available  $V_{S30}$  data in California. Another  $V_{S30}$  model for Taiwan (Kwok et al. 2018) also used terrain-based classifications as well as the more common geology classifications and combined the two models in a weighted fashion.

In NZ, Cousins et al. (1996) compiled geotechnical site class estimates for all strong-motion stations. The site class estimates were based on Standards New Zealand (1992). The geotechnical data used to develop these estimates, however, was sparse or tentative (e.g., based on geologists' estimates without any invasive explorations). Most station information, moreover, was assumed based on regional geology maps.

Destegul et al. (2009) developed a site amplification map for NZ based on geology maps. The map was then validated by comparing map polygons against 687 accelerograph locations where site class was available. (The method of site class assessment for these accelerograph locations in Destegul et al. (2009) is unclear. The work is attributed to Cousins and is unpublished; it may be a continuation of the Cousins et al. (1996) report wherein most site class estimates were derived from geology maps.) Destegul et al. (2009)'s map was developed before completion of the QMAP project (most recent all-NZ geologic map; GNS Science 2016) and therefore based on geologic data from several scales ranging from 1:25,000 to 1:1,000,000. Destegul et al. (2009) also made pragmatic assumptions about the nature of soils confined in narrow valleys: class C was assigned wherever "soil units were narrow and bounded on one or both sides by weak rock." Abrupt geologic transitions were "buffered" (e.g., by inserting a narrow region of class C between polygons of classes B and D).

Perrin et al. (2015) published the first  $V_{S30}$  map for NZ by assigning NZS 1170.5 (Standards New Zealand 2004) site class categories using QMAP categories. The resulting map provided distinct ranges of  $V_{S30}$  corresponding to the well-known site categorization scheme. The Perrin et al. (2015) map also took steps to account for varying  $V_{S30}$  at the edge of geologic basins, applying ad hoc assumptions about lateral extents of basin edges and the dip angle of rock beneath basins. Such decisions were fairly arbitrary by necessity; e.g., dip angle assumption was driven in part by data resolution. The work drew extensively on data for geology correlations with  $V_{S30}$  based on the detailed California data in Borchardt (1994).

## APPROACH AND WORKFLOW

The present study incorporates many of the techniques applied by others in the prior work that has been discussed, including geology-based, slope-based, and terrain-based proxy variables, and geostatistics for honoring local  $V_{S30}$  data. Our work builds on these methods but

additionally adheres to a Bayesian framework for unifying first-order (prior)  $V_{S30}$  and uncertainty ( $\sigma$ ) estimates gleaned from models for other regions with field data in NZ. We also apply more advanced geostatistical methods (Worden et al. 2018) than the typical RK approach. Compared with previous  $V_{S30}$  models for NZ, which have only used geology proxy variables, the present study adds slope and terrain proxy variables, Bayesian statistics, and geostatistics.

The workflow is summarized in Figure 1 with a box for each incremental model developed. Every model assumes lognormal  $V_{S30}$  and is therefore completely specified by two maps: a median  $V_{S30}$  map and a lognormal standard deviation ( $\sigma$ ) map.

A geology-based model is developed by generating a simplified geologic map with categories consistent with Ahdi et al. (2017b) and applying their  $V_{S30}$  estimates from Alaska. A terrain-based model is developed based on DEM-based “terrain categories,” derived from first-order properties of the DEM (local slope, convexity, and texture; Iwahashi and Pike 2007). Terrain categories are generated for NZ and assigned  $V_{S30}$  values using the terrain-based estimates of Yong et al. (2012). Each of these two “prior” models are updated with  $V_{S30}$  data for NZ in a standard Bayesian framework with lognormal conjugate priors and unknown standard deviation (Section 3.3 in Gelman et al. 2014). The geology-based model is modified to incorporate weak correlations between topographic slope and  $V_{S30}$ , similarly to Thompson et al. (2014), Ahdi et al. (2017b), and Parker et al. (2017).

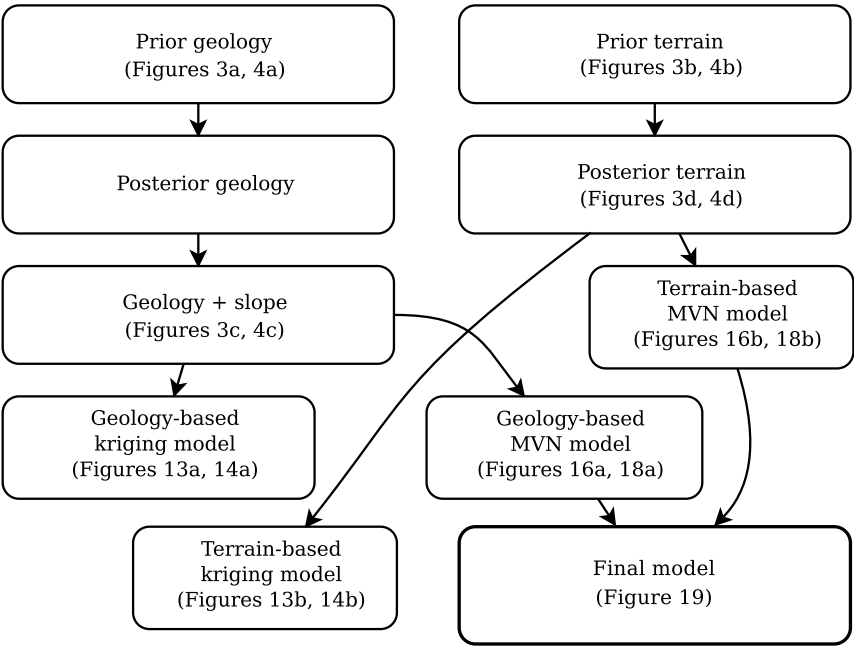


**Figure 1.** Relationships among various model components. Arrows indicate incremental model refinements.

Sample variograms are generated using the residuals corresponding to each of the two constituent models, and theoretical variograms are fitted for forward prediction. Two geostatistical interpolation methods are applied to each of the constituent models: conventional RK and a multivariate approach (MVN; Worden et al. 2018) with a novel additional contribution to automatically and intuitively reduce undesired extrapolation across geologic discontinuities. Finally, a “weighted” model is generated as a statistically weighted combination of the MVN models.

## DATA SOURCES

The information sources used for model development include an NZ geologic map, a topographic map, and  $V_{S30}$  data, as described in the following.

### SURFACE GEOLOGY AND TOPOGRAPHIC DATA

The geologic map, also referred to as QMAP (“quarter-million” for the map scale), is a recent compilation of existing surface geologic maps for regions across NZ (GNS Science 2016). The data are in vector form, with coordinates indicating each corner of approximately 55,000 polygons, each with several metadata fields. Geologic boundaries (polygon edges) are accurate to  $\pm 250$  m. The topographic data source is a DEM developed by LRIS NZ (Landcare Research New Zealand 2010, Barringer et al. 2002) and is available at 25-m resolution. We use the DEM resampled to more manageable 100 and 270-m resolutions for the terrain and slope proxy variables, respectively.

### $V_{S30}$ DATA

The  $V_{S30}$  data are from three data sets, as shown in Figure 2: Kaiser et al. (2017), McGann et al. (2017), and a compilation of recent surface wave–based field investigations in Canterbury. The word “data,” as opposed to “measurements,” is deliberate; most  $V_{S30}$  input data are not from direct measurements. The most striking feature of Figure 2 is the lack of data over most of the country; this is in part because much of NZ is sparsely populated, which has obviated the need for  $V_{S30}$  measurements in most areas. The following paragraphs describe each data set in turn, followed by the assumed measurement uncertainties. A complete tabular listing of input  $V_{S30}$  data is provided in the online supplement.

Kaiser et al. (2017) compiled a list of  $V_{S30}$  values (measurements or estimates) for NZ strong-motion stations. Along with  $V_{S30}$  measurements, qualitative quality rankings (ranging from Q1 = best to Q3 = worst) were provided for each station. Q1 data include both well-constrained surface wave–based methods and invasive methods. Q2 data may be based on well-established local correlations, similar nearby sites, or well-constrained near-surface  $V_S$  profiles that do not necessarily reach 30 m in depth. Q3 values are based solely on estimates, either from preexisting national scale maps (Perrin et al. 2015) or geologists’ estimates. We do not use Q3 data for  $V_{S30}$  modeling here. (Most seismic stations’  $V_{S30}$  estimates are in category Q3 and hence not shown in Figure 2). A number of possible duplicate observations were encountered in the Kaiser et al. (2017) data set, so a preliminary screening was implemented in which duplicates (identified as  $V_{S30}$  points within 2 m of another observation) were removed.

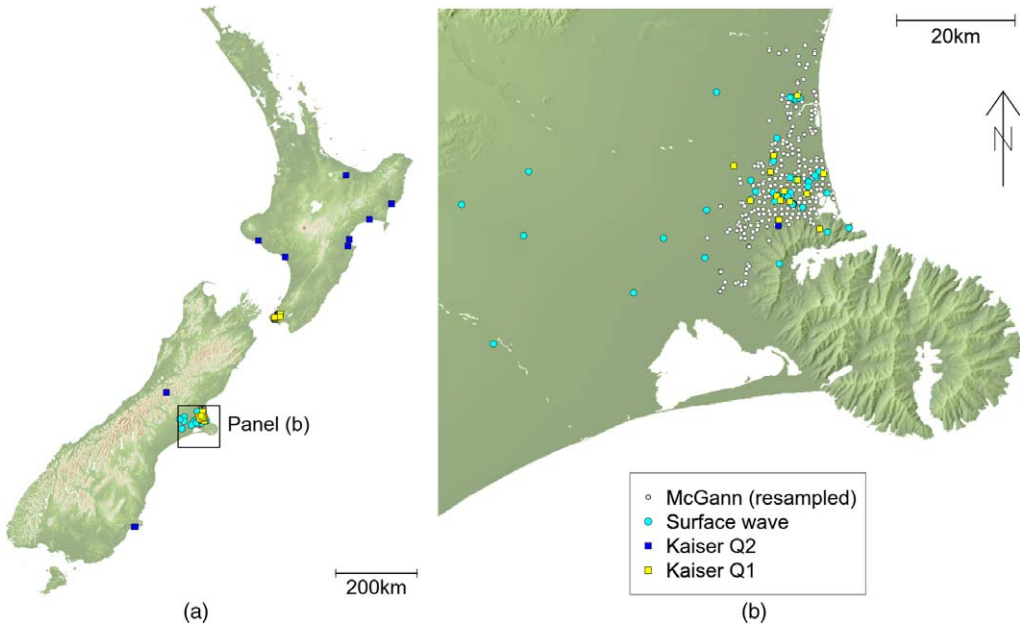


**Figure 2.** (a) Data locations for all of NZ and (b) inset showing Canterbury region for detail. McGann et al. (2017) data were downsampled based on closest proximity to an arbitrary 1-km grid (white circles). Data labeled “Surface wave” (cyan circles) comprise several Canterbury-area surface wave investigations enumerated in the text. The majority of Kaiser et al. (2017) are “Q3” and are not used herein. Kaiser et al. (2017) Q2 (medium quality) and Q1 (highest quality) data are shown as blue and yellow squares, respectively.

McGann et al. (2017) used cone penetration testing (CPT) correlation-derived  $V_{S30}$  values (McGann et al. 2015) to produce a regional  $V_{S30}$  map for the Christchurch area. For our purposes, these data were too numerous (by comparison with the data available for the rest of NZ), and without downsizing would overwhelm the impact of data elsewhere. Accordingly, the McGann et al. (2017) data were resampled from 7,402 points to 280 points by overlaying a 1-km grid and selecting the nearest McGann data point to each gridpoint (Figure 2). This decision was arbitrary but reasonable for the goals of the model development.

The “surface waves” data set refers to a compilation of  $V_{S30}$  data from several surface wave analysis-based site investigations performed following the 2010–2011 Canterbury earthquake sequence (Cox et al. 2011; Wood et al. 2011, 2017; Wotherspoon et al. 2013, 2016; Van Houtte et al. 2014; Teague et al. 2018). Cox et al. (2011) compiled a rapid preliminary report of surface wave testing (multichannel analysis of surface waves (MASW)) performed in Christchurch after the 2010–2011 earthquake sequence along with inverted site profiles from which  $V_{S30}$  estimates were obtained. Wood et al. (2011) and Wotherspoon et al. (2013) performed passive and active surface wave testing at 13 strong-motion stations in and near Christchurch city to obtain  $V_s$  profiles from which  $V_{S30}$  were obtained.  $V_{S30}$  values reported in Wood et al. (2011) have been adjusted in the present work based on updated



analysis of the MASW dispersion curves (Wotherspoon, *pers. comm.*, 2018). Van Houtte et al. (2014) used  $V_{S30}$  values for seven hard sites in an investigation about the role of local seismic attenuation ( $\kappa$ ). The sites'  $V_{S30}$  were inferred from surface wave-based methods using frequencies  $\geq 14$  Hz, meaning that  $V_{S30}$  profiles could not be developed down to 30 m and assumptions were used. Wotherspoon et al. (2016) report seven  $V_{S30}$  values derived from surface wave-based site  $V_s$  profiles measured in conjunction with work by Cox et al. (2014). Deschenes et al. (2018) provide these seven plus two additional  $V_s$  profiles. Wood et al. (2017) evaluated liquefaction case histories at a number of sites with well-characterized  $V_s$  profiles obtained from surface wave-based methods. Not all  $V_{S30}$  profiles extended to 30-m depth; in a few cases where the profiles were within a few meters of 30 m, Wotherspoon (*pers. comm.*, 2018) extended the profiles for  $V_{S30}$  estimates. Teague et al. (2018) developed  $V_s$  profiles at 14 Christchurch sites with deep and complex interbedded geology. Many candidate profiles were generated from the experimental dispersion curves to study epistemic uncertainty associated with the inversions.

## MEASUREMENT UNCERTAINTY

In the subsequent  $V_{S30}$  model development, we use measurement uncertainty quantified as  $\sigma_{\text{meas.}}$ , assuming lognormal distributions. Kaiser et al. (2017) give approximate subjective uncertainty quantities of 10% and 20% for Q1 and Q2 data, respectively. Accordingly, we assigned lognormal standard deviations for measurement uncertainty ( $\sigma_{\text{meas.}}$ ) of 0.1 and 0.2, respectively. All other data are assigned  $\sigma_{\text{meas.}} = 0.2$ . These uncertainties are broadly consistent both with the uncertainties provided by Kaiser et al. (2017) and the general findings of Moss (2008) for  $V_{S30}$  determined from surface wave-based measurements and geology correlations.

## GEOLOGY-BASED AND TERRAIN-BASED MODELS

The development of the geology-based and terrain-based models (in the context of Figure 1) is summarized in Figures 3 and 4 ( $V_{S30}$  and  $\sigma$ , respectively). The individual maps/panels shown in these figures are discussed in detail in the subsequent subsections as they arise. These maps show only the Canterbury region for clarity; the models for all of NZ are available in the online supplement.

### GEOLOGY-BASED PRIOR MODEL

To assign geology-based median  $V_{S30}$  and uncertainty estimates, all map locations first need to be assigned one of a finite number of geologic categories, “flattening” the multi-dimensional textual metadata underlying the geology map into a simpler, “one-dimensional” map (Figure 5a). The geology categories of Ahdi et al. (2017a,b) are selected so that direct comparisons can be made, for straightforward Bayesian updating, and because the geology categories chosen by Ahdi et al. are more specific and discriminating than in many similar studies (and hence more flexible for our application). Ahdi et al. generated  $V_{S30}$  maps for the Pacific Northwest region of North America (Ahdi et al. 2017a) and Alaska (Ahdi et al. 2017b). The categories are enumerated in Table 1.

The 18 geology categories of Ahdi et al. are followed with two exceptions. First, categories G02 and G03 (Fraser river) are discarded because of their regional geologic

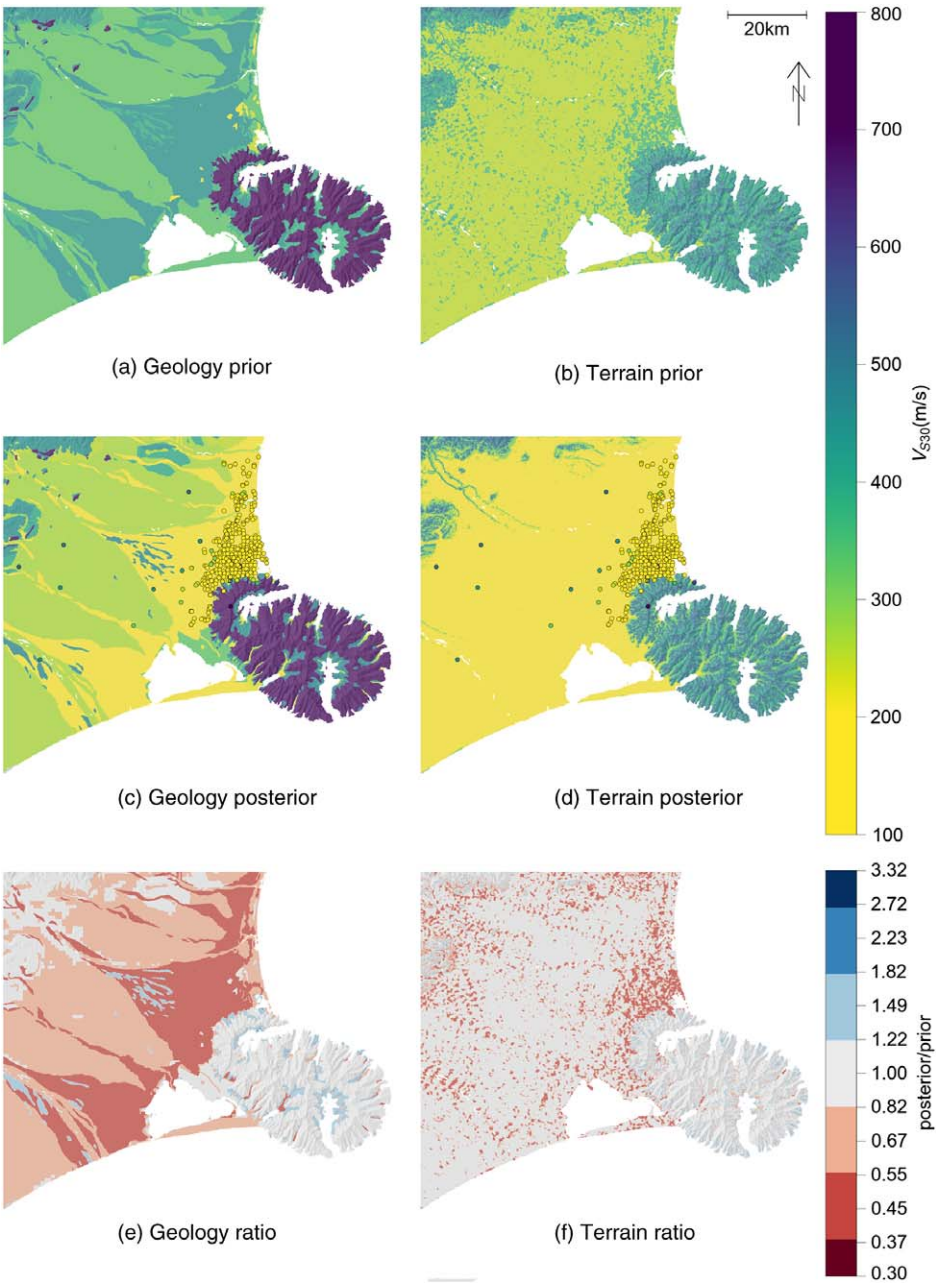


**Figure 3.** Illustrative regional (Canterbury)  $V_{S30}$  maps for various stages of model development: (a) prior geology model; (b) prior terrain model; (c) posterior geology model with slope-based adjustment; (d) posterior terrain model. Comparison of prior to posterior models: (e) ratio of panel (c) to panel (a); (f) ratio of panel (d) to panel (b). Point overlays in (c) and (d) show  $V_{S30}$  measurements used for updating.



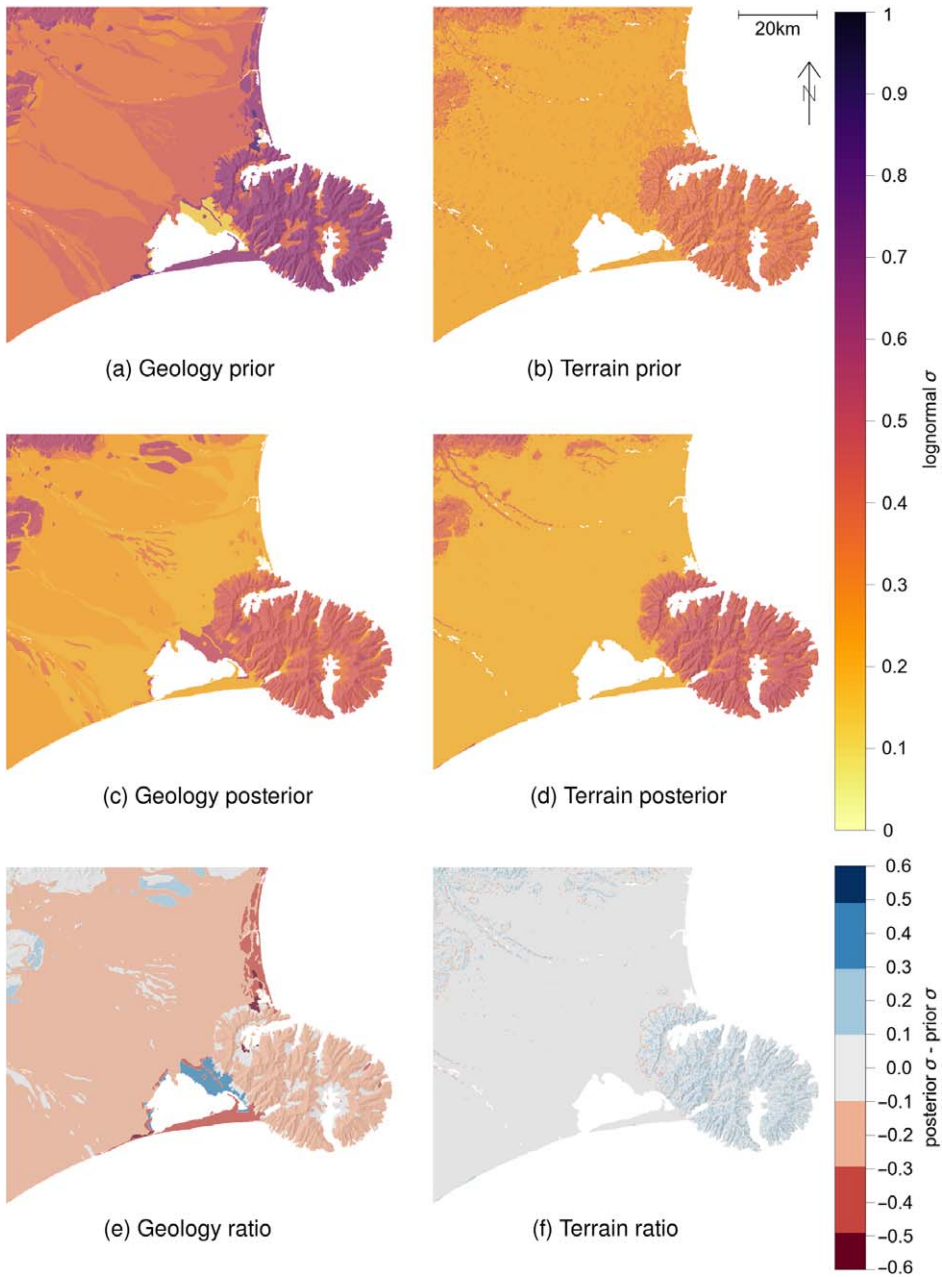


**Figure 4.**  $\sigma$  (sigma) maps for various stages of model development: (a) prior geology model; (b) prior terrain model; (c) posterior geology model with slope-based adjustment; (d) posterior terrain model. Comparison of prior to posterior models: (e) difference between panels (c) and (a); (f) difference between panels (d) and (b).

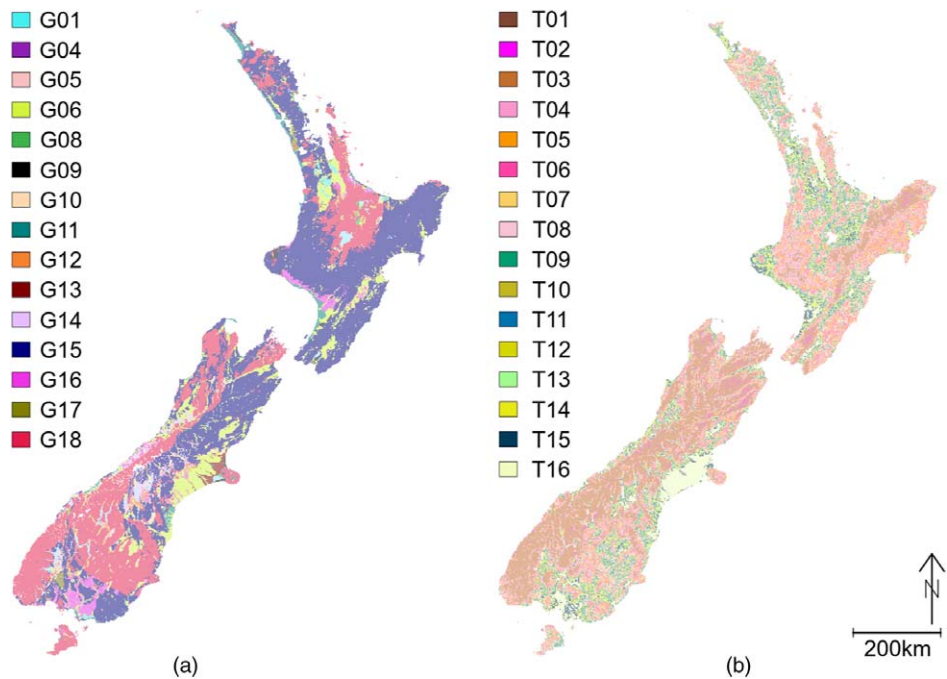


**Figure 5.** (a) Map of geology categories from Ahdi et al. (2017a and 2017b) as applied to NZ. (b) Map of terrain categories from Iwahashi and Pike (2007) as applied to NZ. Terrain colors are selected for direct comparison with Yong et al. (2012).

specificity. Second, categories G07 and G13 (fine and coarse floodplain deposits, respectively) are merged because of the difficulty in distinguishing between the two on the basis of the NZ surface geology metadata. Category G07 is not populated, and all floodplain deposits are lumped together into category G13. Merging these categories is likely more appropriate than retaining the fine/coarse distinction, even if it were practical: Wills and Gutierrez (2009) discuss the reasons that grain size at the ground surface is not generally correlated with grain size over the entire uppermost 30 m for young alluvial deposits.

The categorization process is implemented primarily using a text-based search. Extensive and iterative examination of the metadata fields is performed manually, and five metadata categories are chosen based on the richness of information they carry related to  $V_{S30}$ . The first-order geology-based  $V_{S30}$  model—using  $V_{S30}$  and  $\sigma$  values from Ahdi et al. (2017b)—is shown in Figures 3a ( $V_{S30}$ ) and 4a ( $\sigma$ ). The values assigned to these models correspond to the “prior” columns in Table 1.

### TERRAIN-BASED PRIOR MODEL

Iwahashi and Pike (2007) proposed a method of using a DEM to automatically generate a map of terrain categories that roughly correlate with surface geology, geomorphology, or both. The method relies on successive discrimination based upon three spatial fields:

**Table 1.** Geology categories with  $n$  = number of observations per category and prior and posterior (slope adjusted)  $V_{S30}$  and  $\sigma$  values for each

ID	Description	$n$	$V_{S30}$ (m/s)		$\sigma$	
			Prior	Posterior	Prior	Posterior
G01	Peat	9	161	163	0.52	0.30
G04	Artificial fill	11	198	273	0.31	0.28
G05	Fluvial and estuarine deposits	11	239	200	0.87	0.44
G06	Alluvium and valley sediments	25	323	271	0.36	0.24
G08	Lacustrine (including glaciolacustrine)	0	326	326	0.14	0.50
G09	Beach, bar, dune deposits	70	339	204	0.65	0.23
G10	Fan deposits	5	360	247	0.34	0.34
G11	Loess	4	376	473	0.38	0.35
G12	Glacigenic sediments (drift and outwash)	0	399	399	0.30	0.50
G13	Flood deposits	252	448	197	0.43	0.20
G14	Glacial moraines and till	0	453	453	0.51	0.51
G15	Undifferentiated sediments and sedimentary rocks	0	455	455	0.55	0.55
G16	Terrace deposits and old alluvium	2	458	335	0.76	0.60
G17	Volcanic rocks and deposits	0	635	635	0.99	0.99
G18	Crystalline rocks (igneous and metamorphic)	4	750	691	0.64	0.45

topographic slope, local convexity, and texture. The approach follows a “nested-means” logic (i.e., the categories are divided first on the basis of comparing local slope to mean slope for the entire map domain and then subdivided by convexity and texture). It can be used to generate terrain classes composed of 8, 12, or 16 unique categories, with 12-class and 16-class discrimination achieved by repeated subdivision of the regions with low topographic slope. We followed [Yong et al. \(2012\)](#) in choosing the 16-category implementation; this decision is justified presently in the context of the Bayesian updating step. One advantage of the [Iwahashi and Pike \(2007\)](#) method (in contrast to other similar classification schemes) is that it is “unsupervised,” i.e., no decisions need be made regarding the values (slope, convexity, texture) defining boundaries between terrain classes. One downside of the approach is that these boundary values are based on computing the mean for the map domain, yielding different maps for different domains. This restriction implies that application-specific calibrations are important.

We generated rasters for the [Iwahashi and Pike \(2007\)](#) categories in NZ using the DEM resampled at 100 m (our final target map resolution). (The resolution of the final product is not 100 m in the strictest sense, but in a “neighborhood average” sense. Slope and convexity are both computed for a 9-cell moving window, and texture is computed using a 10-cell radius.) By contrast, the worldwide classification by [Iwahashi and Pike \(2007\)](#) used the 1-km resolution Shuttle Radar Topography Mission DEM (SRTM30; [Farr et al. 2007](#)). Because of both the DEM resolution and the domain-dependent nature of the algorithm, our categories do not precisely match the [Iwahashi and Pike \(2007\)](#) SRTM30-derived

categories for NZ. We expect this to be of trivial consequence, both because of the roughly scale-invariant (fractal) features of landforms and because of subsequent reductions in epistemic uncertainty owing to the Bayesian updating process in the next step (i.e., the application-specific calibration).

The newly generated 100-m resolution terrain category map is shown in Figure 5b. The Iwahashi and Pike (2007) categories are listed with short descriptions borrowed directly from Yong et al. 2012 in Table 2. It must be emphasized that these are mnemonic labels affixed to quantities that are purely statistical in nature; the labels do not carry strong geologic meaning.  $V_{S30}$  and  $\sigma$  values from Yong et al. 2012 (see “Prior” columns in Table 2) are assigned to their corresponding categories from Figure 5b, analogously to the geology-based model, to produce the prior terrain-based model (Figures 3b and 4b).

BAYESIAN UPDATING USING NZ DATA

This section describes the development of posterior models, as shown in the second row of Figure 1. Among the desirable aspects of Bayesian analysis are its amenability to simple verbal descriptions, its agnosticism of the distinction between subjective beliefs and objective data (allowing for a crude “better-than-nothing” formulation of prior beliefs encoded as wide or noninformative prior distributions), and its tendency to demand an explicit accounting of all statistical assumptions being made. Thorough discussions of the semantics of Bayesian theory and analysis are found in D’Agostini (2003) and McElreath (2015). In this work,

**Table 2.** Terrain categories with  $n$ =number of observations per category and prior and posterior (slope adjusted)  $V_{S30}$  and  $\sigma$  values for each

ID	Description	$n$	$V_{S30}$ (m/s)		$\sigma$	
			Prior	Posterior	Prior	Posterior
T01	Well-dissected alpine summits, mountains, etc.	0	519	519	0.35	0.50
T02	Large volcano, high block plateaus, etc.	0	393	393	0.42	0.50
T03	Well-dissected low mountains, etc.	0	547	547	0.47	0.50
T04	Volcanic fan, foot slope of high block plateaus, etc.	0	459	459	0.35	0.50
T05	Dissected plateaus, etc.	2	402	324	0.31	0.41
T06	Basalt lava plain, glaciated plateau, etc.	7	345	301	0.28	0.31
T07	Moderately eroded mountains, lava flow, etc.	3	388	536	0.42	0.38
T08	Desert alluvial slope, volcanic fan, etc.	3	374	515	0.32	0.38
T09	Well-eroded plain of weak rocks, etc.	4	497	284	0.35	0.36
T10	Valley, till plain, etc.	6	349	317	0.28	0.33
T11	Eroded plain of weak rocks, etc.	2	328	267	0.27	0.40
T12	Desert plain, delta plain, etc.	0	297	297	0.29	0.50
T13	Incised terrace, etc.	15	500	217	0.50	0.25
T14	Eroded alluvial fan, till plain, etc.	8	209	242	0.17	0.31
T15	Dune, incised terrace, etc.	166	363	199	0.28	0.21
T16	Fluvial plain, alluvial fan, low-lying flat plains, etc.	170	246	202	0.22	0.21

Bayesian updating is performed on both the geology-based and terrain-based models presented in the previous section. Since Bayesian updating is intuitive, the updating is described here at a high level first. The next section discusses some important implementation details.

Bayesian Updating Summary

To facilitate comparison with the prior models, the ratio of the posterior to prior models’  $V_{S30}$  estimates is presented in Figure 3e and 3f. (Figure 3c and 3e refers to the posterior geology with slope modification, discussed subsequently; this is nearly the same as the posterior geology without slope modification, which is omitted to save space. The difference between the two is trivial enough to disregard momentarily.) The greatest changes to the geology model resulting from the updating process are in the floodplain deposits (category G13) beneath Christchurch city, where  $V_{S30}$  data are abundant and generally lower than for the comparable soil units from Ahdi et al. (2017b) in Alaska. The  $\sigma$  maps corresponding to the posterior geology-based and terrain-based models are shown in Figure 4c and 4d.

The median and standard deviation of each category’s prior and posterior  $V_{S30}$  distributions are concisely summarized alongside the data in Figures 6 (geology) and 7 (terrain). Here, the gray circles represent the NZ  $V_{S30}$  data and are plotted with transparency and a small horizontal “jitter” to reduce overplotting. The red markers and lines indicate the prior model median and  $\pm 1$  standard deviation. The blue markers and lines represent the posterior model median and  $\pm 1$  standard deviation. The prior and posterior median ( $V_{S30}$ ) and standard deviation ( $\sigma$ ) correspond to the  $V_{S30}$  and  $\sigma$  values in the maps in Figures 3 and 4.

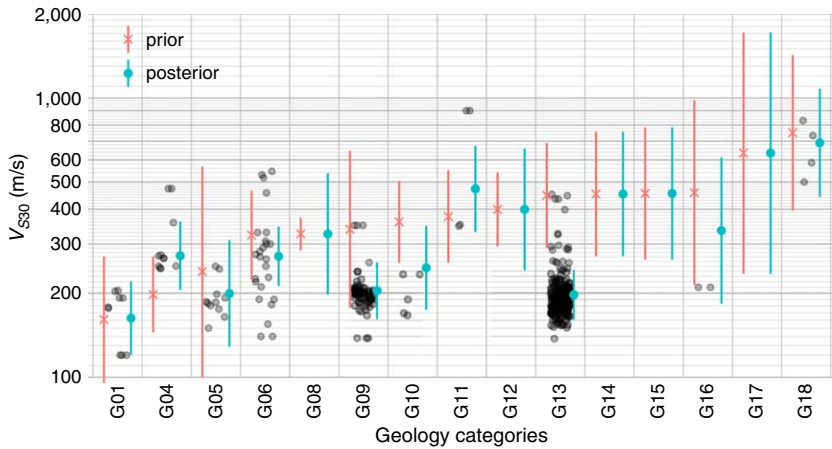


**Figure 6.** Bayesian updating for geology-based model. The colored symbols and lines represent median and  $\pm 1$  standard deviation for lognormal prior (red “x”) and posterior (blue “o”) distributions. The prior distribution is based on Ahdi et al. (2017b). The minimum  $\sigma = 0.5$  criterion is noticeable for categories G08 and G12. Gray dots represent data used for updating.

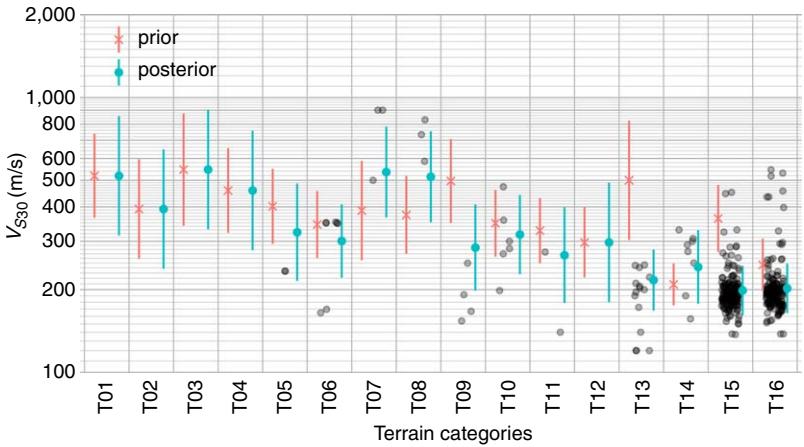


**Figure 7.** Bayesian updating for terrain-based model. The colored symbols and lines represent median and  $\pm 1$  standard deviation for lognormal prior (red “x”) and posterior (blue “o”) distributions. The prior distribution is based on [Yong et al. \(2012\)](#). The minimum  $\sigma = 0.5$  criterion is noticeable for categories T01, T02, T03, T04, and T12. Gray dots represent data used for updating.

The general behavior illustrated in Figures 6 and 7 can be summarized as follows: If the prior model and the data are in stark disagreement, the posterior model represents a “compromise” between the data and prior model, and a larger posterior  $\sigma$  reflects this underlying uncertainty. By contrast, if the NZ  $V_{S30}$  data are tightly clustered around the prior prediction, the posterior  $\sigma$  will tend to be lower than the prior  $\sigma$  to reflect the additional confidence conferred on the model by the data. This can be seen in Figure 4e and 4f. Although much of the map area is negative (indicating a reduction in uncertainty from the prior to posterior models), not every category shows a reduced  $\sigma$ . These are categories where NZ data were sparse or not in good agreement with the prior  $V_{S30}$  values from [Ahdi et al. \(2017b\)](#) or [Yong et al. \(2012\)](#).

The primary difference between Figure 3e and 3f and between Figure 4e and 4f is the lower absolute value in Figures 3f and 4f. This shows that prior distributions were—at least in the Canterbury region—in better agreement with NZ data for the terrain-based  $V_{S30}$  model ([Yong et al. 2012](#)) than for the geology-based model ([Ahdi et al. 2017b](#)). This might suggest that the geology of California is more similar to NZ than the geology of Alaska. Alternately, or additionally, it might simply demonstrate that terrain-based  $V_{S30}$  estimation is inherently less subjective than geology-based estimation.

In the course of developing the terrain-based model, the question arises as to whether the 16-category implementation of [Iwahashi and Pike \(2007\)](#) is superior to the 12-category or 8-category options. In particular, there is the concern of whether or not a 16-category model is “overfitting” available data by comparison with a comparable 12-category or 8-category model. We decided to use 16 categories for two reasons. First, this choice simplifies the updating process. Because [Yong et al. \(2012\)](#) used 16 categories, deviating from this choice



would require us to lump the Yong categories together, introducing another form of epistemic uncertainty related to the categories' spatial distributions and sampling distributions in California and NZ. The second reason for using 16 categories is that it offers the best predictive power given the quantity of data available and its distribution across terrain categories. The motivation for using less than 16 categories would arise only if the 8-category and 12-category schemes result in fewer sparsely populated categories. On the contrary, this is not the case. The [Iwahashi and Pike \(2007\)](#) categories are numbered in order of decreasing topographic slope, and—because of various clustering influences already discussed—the steep categories (generally mountainous/rocky) tend to be more sparsely populated than the shallow categories (generally low-lying/soil). The result of the interaction of these various statistical biases is that the 16-category implementation gives superior discrimination in flatter regions, where  $V_{S30}$  data are plentiful, without splitting the data within any bins that are sparsely populated in the 8-category or 12-category versions.

### Bayesian Implementation Details

The preceding section presented the Bayesian updating process at a high level; this section contains details of the implementation that are useful for replicating our model development, including our application-specific implementation choices. This discussion adheres to the notation in [Gelman et al. \(2014\)](#), pp. 67–69).

The updating presumes normally distributed data (i.e.,  $\ln(V_{S30})$  is normal) with a conjugate prior distribution and unknown variance ( $\sigma^2$ ). Two application-specific decisions are included in the discussion that follows. The first relates to the relative weighting between the prior and the data; the second relates to an arbitrary minimum threshold  $\sigma$  applied before the updating process to avoid overfitting caused by clustered observational data.

A transformation of variables is required to perform lognormal updating using the procedure for normal distributions from [Gelman et al. \(2014\)](#). Each lognormal distribution is completely specified by  $\mu$  (the mean of  $\ln V_{S30}$ ) and  $\sigma$  (lognormal standard deviation).  $\sigma$  is updated assuming a scaled inverse-chi-squared ( $Inv - \chi^2$ ) marginal posterior density.

As discussed, prior distributions are selected for each category using the  $\mu$  and  $\sigma$  values reported in [Ahdi et al. \(2017b\)](#) for Alaska and [Yong et al. \(2012\)](#) for California (Tables 1 and 2, respectively). That is to say, we view the conclusions of [Ahdi et al. \(2017b\)](#) and [Yong et al. \(2012\)](#) (and  $V_{S30}$  data from Alaska and California) as sound bases for first-order estimates of  $V_{S30}$  in NZ, given no other data.

For brevity, we have relegated a summary of the mathematical implementation ([Gelman et al. 2014](#)) of the approach in the online supplement. In our implementation we made application-specific assumptions about the relative weighting between the prior and data. These assumptions are reflected in the choice of initial values for the integer-valued counter variables  $\nu_0$  and  $\kappa_0$  (we set  $\nu_i = \kappa_i$ , which is common but not required). In [Gelman et al. \(2014\)](#),  $\kappa_0 = \nu_0$  represents the “number of observations” contained in the prior. Quotation marks are used to emphasize that the prior is not generally a uniform data set but may be a degree of belief or a combination of qualitative and quantitative elements. The meaning of  $\kappa_0$  and  $\nu_0$  is a step removed from reality: these parameters do not reflect the process applied by [Ahdi et al. \(2017b\)](#) in its entirety, nor do they directly represent the number of physical  $V_{S30}$  measurements in their work. (Indeed, the clustering of  $V_{S30}$  data may mean that unique values

of  $\kappa_0$  and  $\nu_0$  should be chosen for each geologic category, but this is not explored further.) In any case, the choice of  $\kappa_0$  and  $\nu_0$  represents a subjective decision about the appropriateness of applying Ahdi et al. (2017b) models in an NZ context. This “appropriateness” reflects issues of an epistemic nature, such as the quality of  $V_{S30}$  data used in the prior study, the authors’ choices of geologic grouping criteria, the degree to which NZ and California geologic deposits are essentially similar or different, and regional or discipline-specific differences in the naming and classification of deposits by various geologists.

We choose  $\kappa_0 = \nu_0 = 3$  for this application. A geologic category with  $n = 3$  datapoints in NZ would therefore give a posterior distribution based on equal weighting between the data and the prior distribution. Considering the available data, this choice yields a reasonable compromise between the prior distributions and the data (Figures 6 and 7).

A second application-specific decision is made regarding the  $\sigma$  values in the priors. Given that the observational data are sparse and clustered, there is the risk that posterior  $\sigma$  is artificially low because of the influence of clustered  $V_{S30}$  data when the data may not be representative of the entire map domain. To address this, we impose an arbitrary minimum value of 0.5 (natural log scale) on the model priors before applying the updating algorithm. The intent of this threshold  $\sigma$  constraint is to avoid overfitting in categories where  $V_{S30}$  data are few, but of similar value (e.g., terrain category T05 in Figure 7). The results of this can be seen in category groupings that are poorly constrained, such as in geology categories G08 and G12 in Figure 6 as well as terrain categories T01 through T05 and T12 in Figure 7. (Prior distributions shown are those from Tables 1 and 2; the minimum  $\sigma = 0.5$  modification is only visible in the posterior distributions.)

## TOPOGRAPHIC SLOPE-BASED MODIFICATION TO POSTERIOR GEOLOGY MODEL

Following Thompson et al. (2014), Ahdi et al. (2017b), and Parker et al. (2017), the geology-based  $V_{S30}$  model can be refined by capturing any slope dependence in the observed  $V_{S30}$  of the various geologic groupings. To examine the slope- $V_{S30}$  correlations,  $V_{S30}$  values were plotted against topographic slope, computed (Horn 1981) at both 9 and 30-arcsec resolutions for direct comparison with Thompson et al. (2014). (Actual resolutions of the 9 and 30-arcsec maps are about 270 and 900 m, respectively; north-south arcseconds and east-west arcseconds are not similar in NZ.) Thompson and Wald (2012) found that the correlations associated with the coarser 30-arcsec resolution were slightly better than for 9 arcsec, and Thompson et al. (2014) postulated that this might arise because of spurious elevation correlations from nongeomorphic features (vegetation and built infrastructure) resolved at the finer resolution in California. By contrast, in NZ, the finer resolution correlations are the same or slightly better than those for the coarser resolution, and we postulate that the scale of NZ’s built environment is unlikely to impact these correlations in the same way as California. Our slope- $V_{S30}$  correlation is based on 9-arcsec slopes.

Figure 8 shows the correlations of 9 arcsec (270 m) slope with  $V_{S30}$  for four geology categories. Standard least-squares fitting and likelihood testing yield linear relationships along with the  $\pm 2$  standard deviations (95% confidence) bounds shown as dotted lines. Only the geology categories with definitively positive trends are shown, and only these

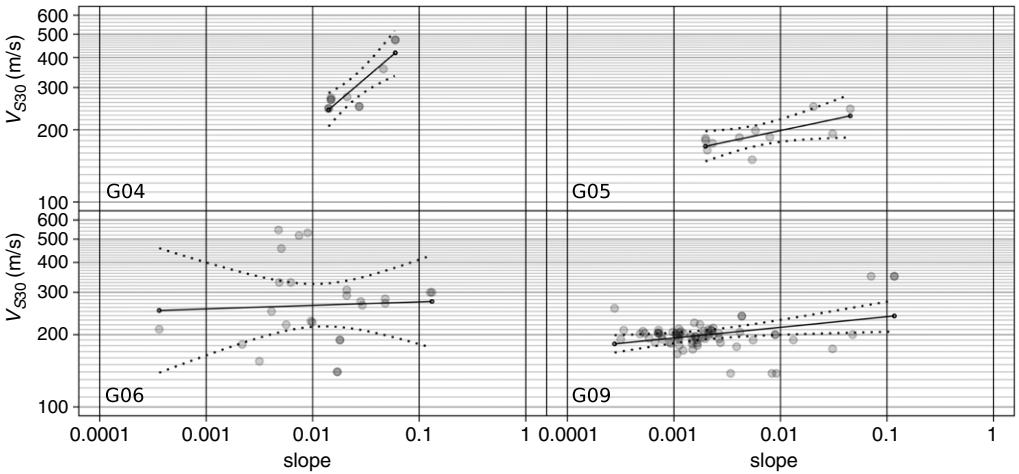


**Figure 8.** Slope dependence of geology-based  $V_{S30}$  model. Slope resolved from 9 arcsec ( $\sim 270$  m) DEM. Only the four geology categories with positive trends are shown. Dotted lines indicate  $\pm 2$  standard deviations (95% confidence bounds) on slope fit.

categories are selected for slope-dependent modification (i.e., the remaining geology categories are modeled with no slope dependence).

The limits of the linear fits in Figure 8 are shown in Table 3. These upper and lower slope ( $\nabla$ ) limits were selected to define continuous piecewise-linear functions (after log transformation) defined by  $(\nabla_0, V_{S30,0})$  and  $(\nabla_1, V_{S30,1})$ :

$$\ln V_{S30} = \begin{cases} \ln V_{S30,0} & \nabla \leq \nabla_0 \\ \ln V_{S30,0} + \frac{\ln(\nabla/\nabla_0)}{\ln(\nabla_1/\nabla_0)} \ln\left(\frac{V_{S30,1}}{V_{S30,0}}\right) & \nabla_0 < \nabla \leq \nabla_1 \\ \ln V_{S30,1} & \nabla_1 < \nabla \end{cases} \quad (1)$$

from which any value of slope yields a single  $V_{S30}$  value that is constrained not to extrapolate beyond the range of observed data. A more sophisticated approach might use logistic curves rather than piecewise-linear and might expend more effort in determining whether the highest and lowest observed slopes are the “best” places to define the inflection points of the function, but we view our approach as simple, objective, and effective.

**Table 3.** Slope adjustment details for categories G04, G05, G06, G09

ID	$\nabla_0$	$\nabla_1$	$V_{S30,0}$	$V_{S30,1}$	$\sigma_{f(\nabla)}$
G04	0.0141	0.0596	242	418	0.14
G05	0.0020	0.0452	171	228	0.31
G06	0.0004	0.1316	252	275	0.24
G09	0.0003	0.1171	183	239	0.22

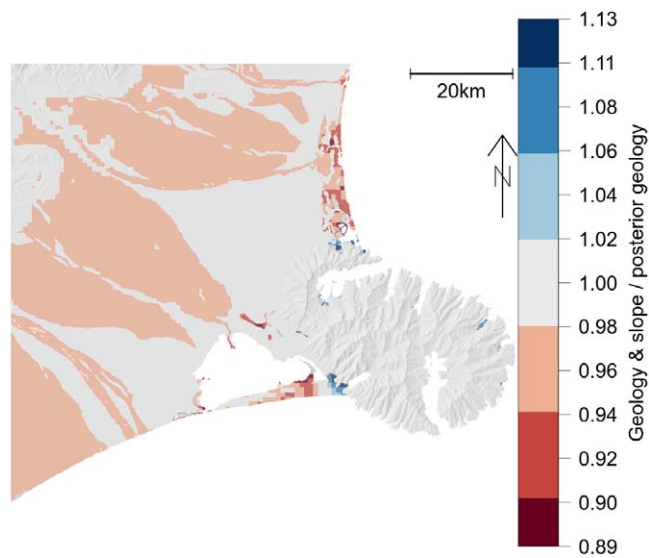


**Figure 9.** Ratio of slope+geology model (Figure 3c) to posterior geology model (not shown) median estimates. Note the small range on the graphic scale indicating a much smaller model change by comparison with the posterior geology update.

In Bayesian parlance, the application of slope correlations to the model is another instance of “updating,” in which a model is improved based on the use of data that were not accounted for beforehand. The posterior  $V_{S30}$  predictions are given by the piecewise-linear trends.

The results of slope-based correction represent a small change from the posterior geology model (by comparison with the prior geology model; compare  $\sigma$  values in Table 3 with those in Table 1). The slope-based  $V_{S30}$  and  $\sigma$  maps are visually indistinguishable from the posterior geology model, so only the log of the ratio of the two models’ median  $V_{S30}$  predictions is presented here (Figure 9). The slope-updated geology model is shown in Figures 3c ( $V_{S30}$ ) and 4c ( $\sigma$ ). Hereafter, we refer to this model as simply the “geology-based” model.

**COMPARING GEOLOGY-BASED AND TERRAIN-BASED MODELS**

Quantitative comparisons of the two posterior model predictions are presented in Figures 10 (mapped prediction comparison for all NZ) and 11 (per-datapoint residual comparison). In the map-based prediction (Figure 10), it is evident that the places where the models disagree most (e.g., the volcanic Taupo and Rotorua area in the central North Island, indicated by a box in Figure 10) are places characterized by unique surface geology and geomorphology, where there is consequently a unique pairing of geology and terrain categories. The model can benefit from data in these locations.

Figure 11 shows normalized geology and terrain model residuals  $\zeta$  on the x and y-axes, respectively:

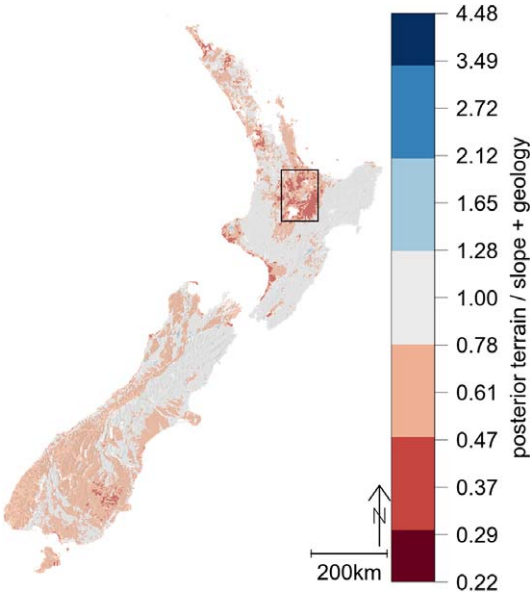


**Figure 10.** Map comparing median  $V_{S30}$  for posterior geology-based and terrain-based models. The Taupo and Rotorua region (boxed) is an example of a region with unique interaction between the geology-based and terrain-based categories that may merit prioritization for future field investigations.

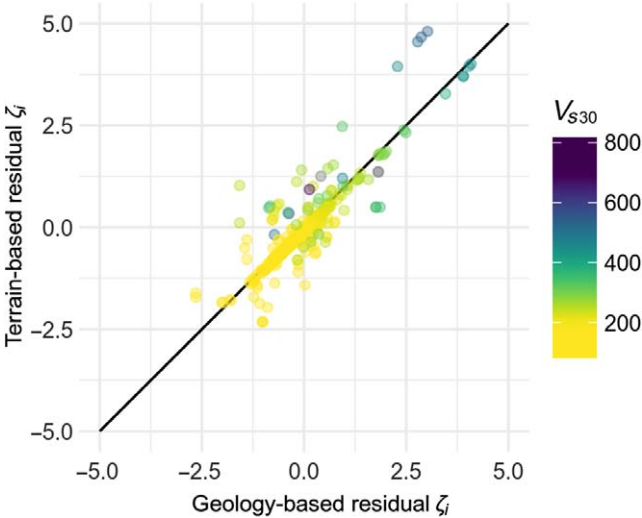


**Figure 11.** Scatterplot comparing  $V_{S30}$  residuals for posterior geology-based and terrain-based models. Colored by  $V_{S30}$ .

$$\zeta_i = \frac{\ln V_{S30_{obs,i}} - \ln V_{S30_{pred,i}}}{\sigma_i} \quad (2)$$

$\sigma_i$  values correspond to the values in Figure 4c and 4d. The residuals are roughly symmetrically scattered across the 1:1 line, suggesting that there is no systematic advantage of the geology-based model over the terrain-based model, or vice versa, after Bayesian updating. Coloring of the points is by measured  $V_{S30}$  and highlights some biases in individual categories, particularly rock categories, which are poorly represented.

## GEOSTATISTICS APPLICATION TO POSTERIOR MODELS

The geology and terrain models developed in the previous section predict  $V_{S30}$  as functions of surface geology, local topographic slope, and terrain proxy variables. A shortcoming of these models is that they do not offer improved predictions in the vicinity of existing measurements. The tool for addressing this issue is geostatistics. Two geostatistical approaches are applied to the geology and terrain models in this section. The first and simpler of the two is regression kriging (RK). The second is the so-called “multivariate normal” (MVN) method (Worden et al. 2018). Both methods are presented and discussed for comparative purposes; the MVN approach is ultimately chosen as the superior method for reasons discussed presently.

In the following sections, first, a concise review is given of the broad aspects of geostatistical approaches, wherein quantifiable geospatial phenomena are modeled as stationary random processes, and the parameterization (i.e., variance and autocorrelation) of the stationary random processes are inferred from variogram analysis. Next, the aspects of the MVN approach that depart from kriging, and its advantages for this work, are highlighted. Aspects of variogram and correlation function selection are discussed in the context of the  $V_{S30}$  map. The results of applying both RK and MVN are presented. The problem of interpolating/extrapolating residuals for a lognormal process such as  $V_{S30}$ , which can result in unreasonably high  $V_{S30}$  estimates in some situations, is discussed. Finally, we present two unique approaches we implemented to ameliorate these issues in a more-or-less automated way that requires few subjective decisions for implementation.

## PRELIMINARIES

This discussion follows notation from Diggle and Ribeiro (2007). The most common assumption underlying geostatistical methods is that spatial fluctuations in an earth science system (e.g.,  $V_{S30}$ ) can be modeled as a Gaussian random process,  $S(\mathbf{x})$ , a 2-D function wherein a set of observations  $S(\mathbf{x}_1, \dots, \mathbf{x}_n)$  for  $n$  locations  $\mathbf{x}_1, \dots, \mathbf{x}_n$  is assumed to be drawn from a multivariate Gaussian (normal) distribution. A Gaussian random process is defined completely by its mean function  $\mu(\mathbf{x}) = E[S(\mathbf{x})]$  and its covariance function  $\gamma(\mathbf{x}, \mathbf{x}') = \text{Cov}\{S(\mathbf{x}), S(\mathbf{x}')\}$ . If the mean is constant and the covariance structure is formulated solely as a function of distance (i.e.,  $\mu(\mathbf{x}) = \mu$  and  $\gamma(\mathbf{x}, \mathbf{x}') = \gamma(\mathbf{u})$  where  $\mathbf{u} = \mathbf{x} - \mathbf{x}'$ ), then the process is known as the special case of a stationary random function (SRF). Usually, SRF are also assumed to be isotropic, i.e.,  $\gamma(\mathbf{u}) = \gamma(\|\mathbf{u}\|) = \gamma(u)$  where  $\|\cdot\|$  designates Euclidean distance. The variance of an SRF is constant:  $\sigma^2 = \gamma(0)$ . Hereafter, we discuss



only functions of scalar  $u$  rather than vector difference  $\mathbf{u}$ , as our application assumes isotropy as is typical for regional applications (e.g., [Thompson et al. 2014](#)).

For the stationary case, the variogram function is an alternative representation of the covariance function:  $V(\mathbf{x}, \mathbf{x}') = \frac{1}{2} \text{Var}\{S(\mathbf{x}) - S(\mathbf{x}')\}$ . This reduces to  $V(u) = \sigma^2\{1 - \rho(u)\}$ , where  $\rho(u) = \frac{\gamma(u)}{\sigma^2}$  is the correlation function, again for the stationary case. The correlation function is 1 for  $u = 0$  (for the typical application where the nonspatial component of randomness is zero) and decreases monotonically to approach zero asymptotically with increasing  $u$ .

The variogram is useful both for interpreting observed spatial processes and for generating predictions using models with SRF. The aforementioned formulation is known as the theoretical variogram. For using observational data to parameterize a geostatistical model, the sample variogram or empirical variogram can be obtained and then used to guide selection of the theoretical variogram. Observational data  $\mathbf{Y}$  are assumed to be of the form  $Y_i = S(\mathbf{x}_i) + Z_i$ , where  $Z_i$  are mutually independent and identically distributed with zero mean and variance  $\tau^2$ . The sample variogram is as follows:

$$V_Y(u_{ij}) = \frac{1}{2} \text{E}[(Y_i - Y_j)^2] \quad (3)$$

The functional form for fitting a theoretical variogram is the following:

$$V_Y(u) = \tau^2 + \sigma^2\{1 - \rho(u)\} \quad (4)$$

This formulation is more general than the one previously introduced, with the addition of the  $\tau^2$  term.

The intercept,  $\tau^2$ , is known as the nugget variance. It represents the nonspatial component of randomness in the process, requiring a dual interpretation of physical meaning, which we discuss presently to contrast conventional kriging with MVN.  $\sigma^2$  is the signal variance. The asymptotic value,  $\tau^2 + \sigma^2$ , is known as the sill and is the variance of the observed process  $Y(\mathbf{x})$ . For the common special case of  $\tau^2 = 0$ , the sill is equivalent to the signal variance. The range of the variogram is the distance  $u$  beyond which there is no change in  $V(u)$ .

## EMPIRICAL VARIOGRAMS

Two theoretical variograms, one each for the geology-based and terrain-based models, are selected by fitting to empirical data. One of the simplest and most common functional forms is chosen for the theoretical variograms, the exponential model:

$$V(u) = \exp\left(-\frac{u}{\phi}\right) \quad (5)$$

where  $\phi$ , the range or shape parameter, is measured in units of distance. The practical range, the value of  $u$  for which  $\rho(u) = 0.05$ , is approximately  $3\phi$  ([Diggle and Ribeiro 2007](#)).

The empirical variograms here are produced with normalized residuals ( $\xi_i$ , Equation 2) in lieu of observations  $S(\mathbf{x}_i)$ . Normalization ensures homoscedasticity of the residuals

**Table 4.** Data subsets used for variogram fitting

Subset	Description	<i>n</i>	Weighting
GS1	<a href="#">Kaiser et al. (2017)</a> Q1 and Q2; no Canterbury data	49	0.5
GS2	<a href="#">Kaiser et al. (2017)</a> Q1 and Q2 and surface wave-based data	127	0.25
GS3	<a href="#">McGann et al. (2017)</a> data (resampled to 1 km)	266	0.25
TS1	Same as GS1 but with terrain categories T15 and T16 removed	29	0.5
TS2	Same as GS2 but with terrain categories T15 and T16 removed	42	0.5

(e.g., [Jayaram and Baker 2009](#)), which is necessary to ensure the geostatistical assumption of Gaussian stationarity.

Because of the highly clustered nature of the available  $V_{S30}$  data, we explore several subsets of the data to assess the sensitivity of the fitted theoretical variogram to the data underlying the empirical variogram. The selection of subsets is motivated by a hypothesis that the large scale and relative spatial uniformity of the Canterbury plains—the largest alluvial deposit in NZ—may yield a variogram with a range that is longer than appropriate for other geographic regions. Thus we examine subsets with various degrees of exclusion of  $V_{S30}$  data from Christchurch or Canterbury. These are summarized in Table 4.

Preliminary examination of the empirical variograms led us to conclude that the geology model yielded fairly “well-behaved” variograms, while the terrain model variograms were considerably less smooth. We postulated that since the geology model incorporates continuously varying slope correction functions for a few hand-selected geologic categories, whereas the terrain model subdivides regions based on discrete slope bins using the [Iwahashi and Pike \(2007\)](#) method, the latter might show some arbitrary stochasticity in the pairwise empirical variogram ordinates, particularly in categories T15 and T16 (which are the most prevalent in the Canterbury plains and other wide alluvial basins). The terrain subsets were modified by removing all points from terrain categories T15 and T16, and the resulting theoretical fits were improved.

The final selections for the geology-based and terrain-based model variograms are summarized in Figure 12. For each of the five subsets, a logarithmically spaced binning scheme was chosen and pairwise variogram ordinates were averaged within each bin to generate an unbiased estimator of the theoretical variogram. The 95% confidence intervals obtained by bootstrapping are shown for each bin. The judgment-based weighting factors shown in Table 4 were used to fit one final exponential variogram each to the geology-based and terrain-based models by weighted least-squares minimization ([Pebesma 2014](#)). Notably, inspection of the plots reveals that the variogram is fairly insensitive to the data subsetting schemes we evaluated. The effective ranges for the geology and terrain variograms are 4.2 and 3.0 km, respectively. We note that since the variograms are calibrated to the normalized model residuals their differences are not necessarily attributable to physical meaning.

**KRIGING**

“Predicting” unobserved values of a spatial process on the basis of geostatistics entails interpolating the observed values with interpolation weights derived from the variogram and

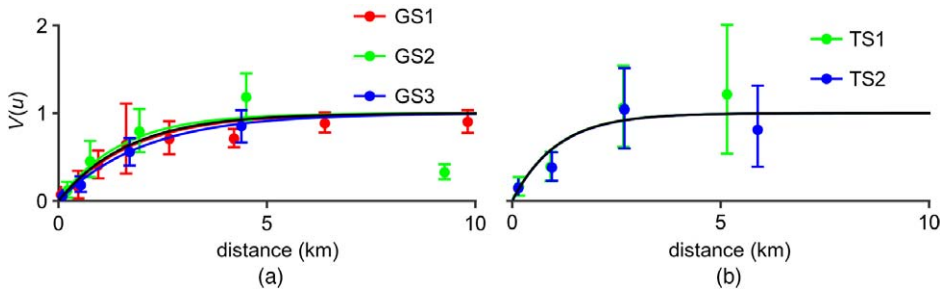


**Figure 12.** Theoretical variogram selection for (a) geology-based models and (b) terrain-based models.

assuming that the mean of the process tracks the observed values. This process is known as kriging. RK (e.g., [Thompson et al. 2014](#)) is an approach that makes the stationarity assumption useful for a wider variety of problems in which the model mean  $\mu = \mu(\mathbf{x})$  is not constant across the problem domain. For RK, consistent with variogram development, the kriging is done on normalized observation residuals,  $\zeta_i$ , assuming that the residual surface is the mean surface of an SRF.

The kriged geology-based and terrain-based  $V_{S30}$  maps are shown in Figure 13. While the new  $V_{S30}$  estimates appear reasonable in general, we wish to highlight one location where this is not the case: a datapoint in Rakaia (identified by a box in Figure 13a). Here, the geology model predicts unrealistically high  $V_{S30}$  values because a high-valued observation (presumably reflective of loess deposits, category G11) appears to be located near a geologic boundary on a lower-valued polygon (G06 or G13) yielding a higher normalized residual

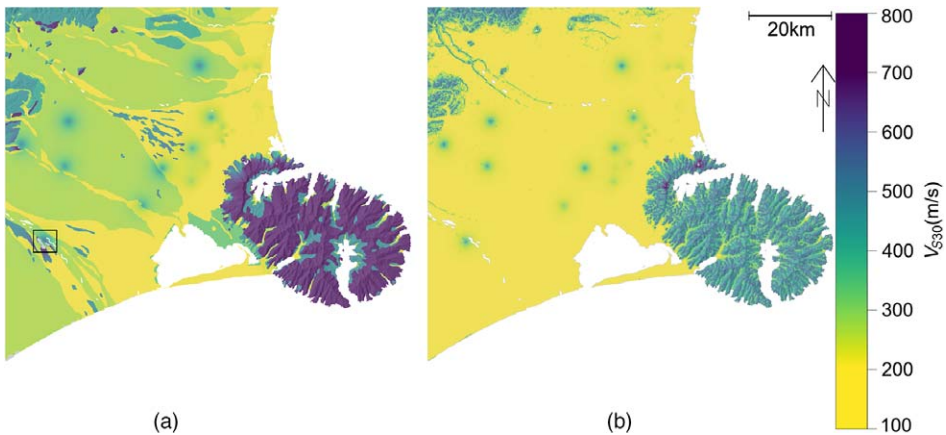


**Figure 13.** The kriged  $V_{S30}$  maps for the (a) geology-based and (b) terrain-based models. An example of potentially inappropriate extrapolation across geologic boundaries is visible in the Rakaia area (boxed).

than may be appropriate. The smoothed residual surface is multiplicative rather than additive, owing to the lognormal assumption, and consequently exerts a great influence over the area. (A tiny region in the vicinity of this error is colored gray, indicating the color scale is “clipped,” i.e., the model predicts a median  $V_{S30}$  in excess of 1,000 m/s.)

This issue is exemplary of geostatistical problems that may occur wherever observational data happen to be located on the “wrong side” of a high-contrast geologic boundary (between cemented loess and unconsolidated sediments in this example or between rock and soil generally). In the next section, we propose a novel method of handling such errors that is effective at reducing undesirable cross-boundary extrapolation in lieu of the time-consuming and subjective alternative approach (i.e., manually identifying and relocating problematic observations or map boundaries wherever this issue arises).

The kriged uncertainty ( $\sigma$ ) maps are shown in Figure 14 and, as expected, approach zero near measurements because the nugget of the variogram is zero. The “background”  $\sigma$ , in regions where there are no nearby observations, reverts to the input  $\sigma$  (i.e., Figure 4).

The kriged residual in Figure 14 suggests that the baseline model may systematically underpredict  $V_{S30}$  in the Canterbury plains, west of Christchurch city. This is not unexpected; in the simplified geology categories (Figure 5a), there is no discrimination between the surface geology beneath Christchurch and that in the plains to the west. But the geology of the coastal basin consists of interbedded layers from alternating deposits of river/alluvial and marine deposits, which may suggest that surface geology alone (presuming it is representative of less than 30-m depth) is inadequate as a proxy for  $V_{S30}$ . This dilemma with young alluvial deposits is common for  $V_{S30}$  estimates that rely on surface geology (e.g., [Wills and Gutierrez 2009](#)).

Related to this issue is the dominance of the Christchurch city data. An alternative approach would be to generate another model by choosing a sparser sampling distance

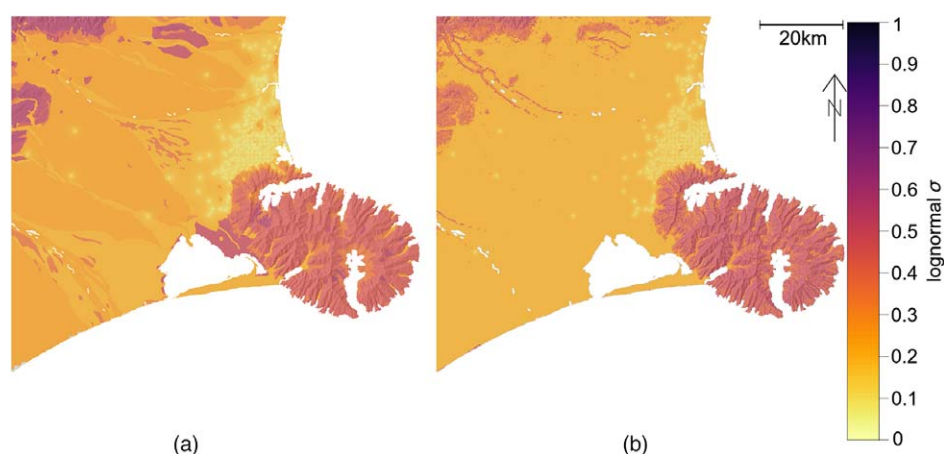


**Figure 14.** The kriged  $\sigma$  maps for the (a) geology-based and (b) terrain-based models. Lower uncertainty corresponds to locations of  $V_{S30}$  data (Figure 2).

for the Christchurch data and thereby decreasing the weight accorded to urban data. Ultimately, this decision represents a trade-off that should be informed by application. Our view is that  $V_{530}$  data density is generally correlated with population density for good reason, and for engineering applications, it is acceptable to allow data to drive the model, irrespective of the unavoidable spatial clustering.

## MVN METHOD

Worden et al. (2018) present a more generalized geostatistical approach than kriging, which we refer to as the multivariate normal (MVN) method. The primary advantage of this method in our work (compared with RK) is that it allows for assumptions about measurement uncertainty to be applied on a location-by-location basis.

In conventional kriging, if the nonspatial component of variance—the nugget—is zero, then the interpolated mean surface is constrained to match the observational values at their respective locations. A nonzero nugget means that the interpolated surface need not honor the data precisely. The nonzero nugget has a dual physical meaning: on the one hand, the tendency of the modeled system to exhibit spatial discontinuities, and on the other hand, measurement uncertainty. In practice, these causes are rarely disentangled because many collocated measurements would be required. A nonzero nugget in the variogram is formally equivalent to modeling the measurement process as a Gaussian spatial process with a discontinuity at the origin of the correlation function. But importantly, in conventional kriging, a nonzero nugget is the same across the problem domain. By contrast, in the MVN approach, explicit assumptions about measurement uncertainty are enforced via “correlation adjustment factors” that can be assigned to measurements on an individual basis. The output  $\sigma$  can be different at different data points in accordance with the respective input measurement uncertainties. Correspondingly, individual observations exert a “pull” on the interpolated surface that is inversely correlated with measurement uncertainty. The variogram nugget is thus effectively localized for data from different sources. (The MVN results reduce to be equivalent to the kriging results with zero nugget for the special case where all measurement uncertainties are set to zero.)

We assigned each input datum a lognormal measurement uncertainty,  $\sigma_{meas.}$ . These values were chosen following the discussion in the *Data Sources* section and are tabulated in the online supplement. Assigning  $\sigma_{meas.}$  is not trivial or objective (e.g., McElreath 2015). However, given that measurement uncertainty is a “nuisance parameter,” in the parlance of Gelman et al. (2014, pp. 63–64), it is intuitive to expect that the chosen value of  $\sigma_{meas.}$  becomes insignificant in regions of dense data (e.g., Christchurch city) and therefore impacts the model most strongly in regions with little data. Moreover, this framework allows for future model refinements on the basis of more and better observational data.

## Correcting Overpredictions from Cross-Boundary Extrapolation

The issue of “cross-boundary extrapolation” was discussed earlier as it pertains to RK. Here, we propose a novel solution that entails modifying the correlation function  $\rho(u)$  for every unique pairwise combination of locations in the problem domain. To this end, a coefficient is introduced: the “covariance reduction factor” (CRF) with a value between 0 and 1. The CRF is a function of the “difference” between two points of interest. Qualitatively, in this

context, “difference” implies the appropriateness in general of assuming nonzero correlation between two locations irrespective of their separation distance. Quantitatively,  $0 \leq \text{CRF} \leq 1$ .

A proxy variable needs to be selected to choose CRF given two locations,  $\mathbf{x}_1$  and  $\mathbf{x}_2$ . We chose the ratio of the two corresponding model  $V_{S30}$  predictions, since this reflects the most pertinent information contained in both the geology-based and terrain-based models. Alternatives could be chosen, for example, the ratio of slopes alone or a more complex assessment of the geologic map. The function for CRF is chosen as follows:

$$\text{CRF} = \exp\left(-a \left| \ln \frac{V_{S30_1}}{V_{S30_2}} \right| \right) \tag{6}$$

which ensures  $\text{CRF} = 1$  for  $V_{S30_1} = V_{S30_2}$  with exponential decay as the ratio of the baseline  $V_{S30}$  estimates decreases. We selected  $a = 1.5$  based on the heuristic that the decay function ought to yield  $\text{CRF} \approx 0.1$  (i.e., almost no correlation) for the ratio  $\frac{V_{S30_1}}{V_{S30_2}} \approx 5$ ; see Figure 15. This corresponds to an arbitrary reference hypothetical in which  $V_{S30_1} = 1,000$  m/s and  $V_{S30_2} = 200$  m/s, i.e., “rock” and “soil.” This heuristic is necessarily arbitrary and reflects an intuition about the complexity of geologic processes that depart from idealized assumptions underlying geostatistical methods. While there are alternative approaches to representing this complexity, the proposed method appears to handle the issues well globally and relies on the selection of only a single parameter. This is desirable for updating the model in a more-or-less automated fashion in the future as additional data are incorporated into the model.

To apply this modification to the MVN method, CRF is computed in accordance with Equation 6. Then Equation 7 from Worden et al. (2018) is adjusted by defining a modified correlation coefficient:

$$\rho'_{Y_iY_j} = \rho_{Y_iY_j} \text{CRF}_{Y_iY_j} \tag{7}$$

Results

The result of the covariance-weighted MVN application is presented in Figure 16. The ratios of the results in Figure 16 to the RK models (Figure 13) are shown in Figure 17.  $\sigma$  for the covariance-weighted MVN model is shown in Figure 18.

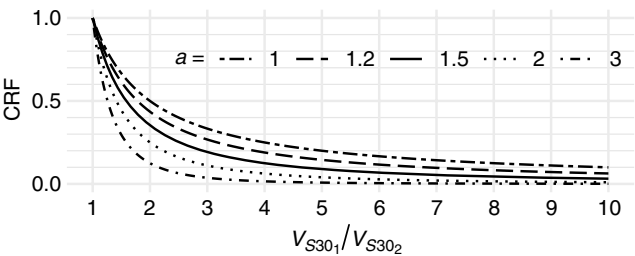
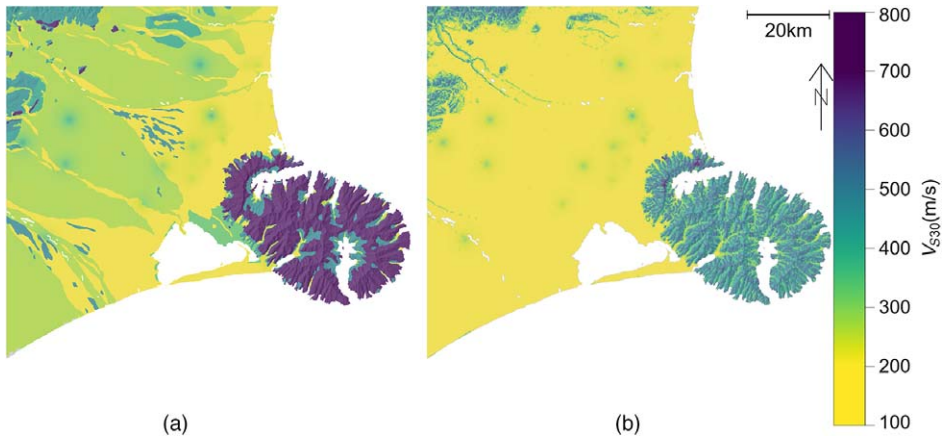


Figure 15. Several example covariance reduction functions.





**Figure 16.** Covariance-adjusted MVN model  $V_{S30}$  estimates for (a) geology-based and (b) terrain-based models. The overprediction noted in the RK (Rakaia area, Figure 13) is eliminated.



**Figure 17.** Covariance-adjusted MVN model  $V_{S30}$  predictions compared with RK predictions for (a) geology-based and (b) terrain-based models.

Three items are noteworthy in comparing the performance of the RK and MVN methods (Figure 17):

1. In regions where data are dense, such as Christchurch city, the models yield virtually the same predictions. The collocation of many  $V_{S30}$  datapoints results in a smoothing effect whose details are largely unchanged by the addition of measurement uncertainty.
2. In regions where data are sparse, such as the rural Canterbury plains, the models are slightly different in the vicinity of data because of the way RK and MVN differ in handling measurement uncertainty. The baseline  $V_{S30}$  estimate (geology or

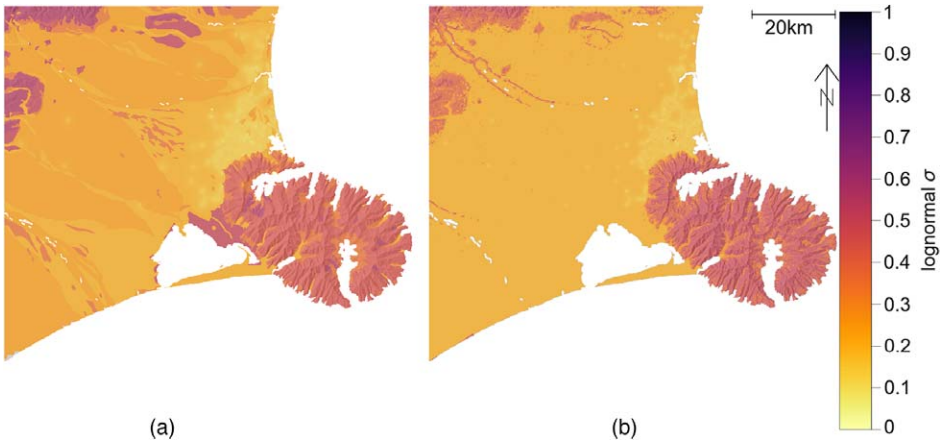


**Figure 18.** Covariance-adjusted MVN model  $\sigma$  for (a) geology-based and (b) terrain-based models.

- terrain model) has no effect at the precise location of an observation for RK, whereas the observation and baseline model estimates are combined in the MVN method, with the proportional influence being a function of the assumed measurement uncertainty.
3. The localized overprediction in the Rakaia area, noted previously, has been resolved by the MVN method. The different degrees of covariance applied across the geologic boundaries in this area are clear in Figure 17a.

### MERGING GEOLOGY AND TERRAIN MODELS

To summarize the preceding discussion, the MVN method is more general and more statistically sound than RK because it allows pointwise assignment of measurement uncertainty, albeit at the expense of longer computation time. The “covariance reduction” method proposed is a transparent and automated way of handling potentially misleading extrapolation of normalized residuals across geologic boundaries. Consequently, we present the MVN model versions as superior to the more conventional RK results. In this section, we combine the geology-based and terrain-based models into a final model.

Having conditioned each constituent model on available data and applied geostatistical interpolation, we see no reason to favor one model over the other and assign each a weighting of 0.5. The decision to weight the two models equally, rather than favoring one over the other, is motivated by the assumption that aspects of the geology-based and terrain-based approaches are mutually complementary. For example, the geology categories can convey information pertaining to  $V_{S30}$  that may not be readily discriminated by the terrain categories, but the terrain data are more spatially uniform, less subject to human interpretation, and may indicate finer detail in local  $V_{S30}$  variations and more accurate velocity contrast boundaries, particularly in areas where the geology map is derived from digitizing older regional-scale maps.

The weighting is done as follows:

$$V_{S,30_{final}} = \exp\left(\sum_{i=1}^n w_i \ln V_{S,30_i}\right) \quad (8)$$

where in general  $\sum_i w_i = 1$  and in the present application (combining two equally weighted models)  $n = 2$  and  $w_1 = w_2 = 0.5$ . The combining of uncertainty represents a “mixture problem”: If the constituent models predict similar  $V_{S30}$  and have small  $\sigma$ , then the resulting  $\sigma$  is a compromise between the two input  $\sigma$  values. On the other hand, if the two models predict significantly different  $V_{S30}$  values, then the combined uncertainty is high, even if the constituent models have low  $\sigma$ :

$$\sigma_{final}^2 = \sum_{i=1}^n w_i \left( \left( \ln V_{S,30_i} - \ln V_{S,30_{final}} \right)^2 + \sigma_i^2 \right) \quad (9)$$

where again,  $n = 2$  and  $w_1 = w_2 = 0.5$ . Once more, this is functionally equivalent to Bayesian updating with equal weighting of “prior” (geology-based model) and “data”

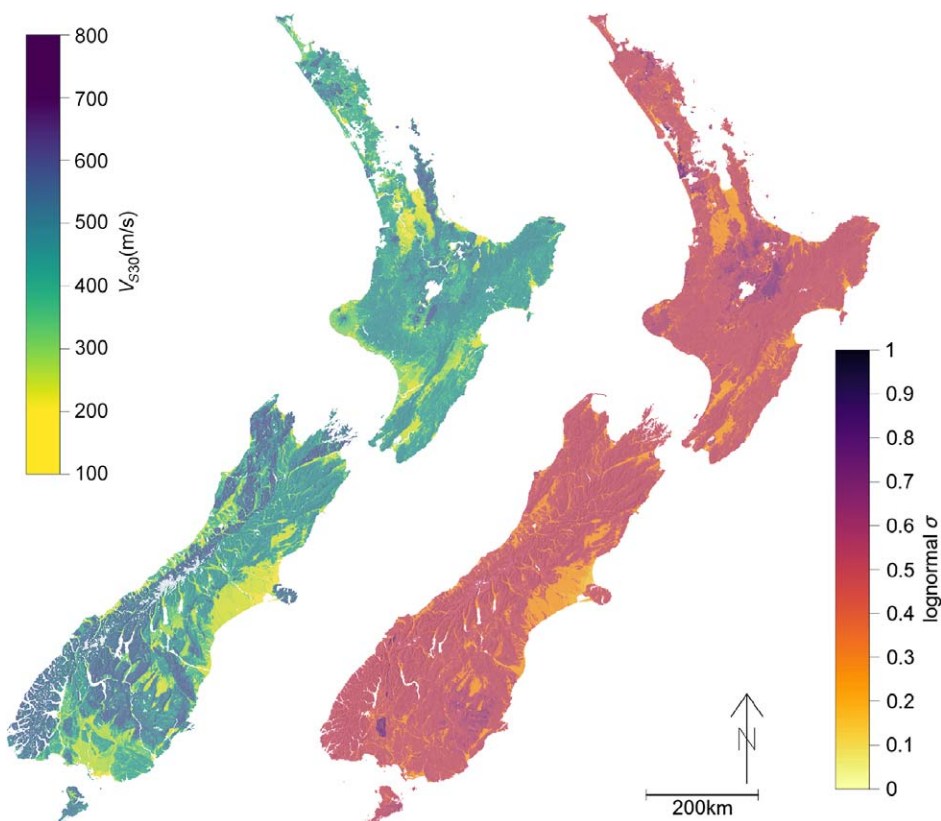


**Figure 19.** (a)  $V_{S30}$  and (b)  $\sigma$  for the final weighted model.

(terrain-based model; e.g., [McElreath 2015](#)). The weighted, final model median  $V_{S30}$  estimate and lognormal  $\sigma$  are presented in Figure 19.

## CONCLUSIONS

A  $V_{S30}$  model for NZ has been developed. The salient features of the model include a fine (100 m) resolution; making use of both geology and terrain covariates; a consistent, local  $V_{S30}$  data inclusion via a transparent and readily updateable Bayesian framework; lognormal standard deviations alongside median  $V_{S30}$  estimates; and a novel modification to the MVN method ([Worden et al. 2018](#)) that reduces covariance for observation-prediction pairs that cross geologic/geomorphic boundaries, yielding heuristically sensible  $V_{S30}$  estimates near these boundaries. The model represents an improvement over recent  $V_{S30}$  models for NZ, which have used geology proxy variables but have not quantified uncertainty or employed geostatistical methods.

The model can be updated relatively easily, and it is expected that recent field work performed in Nelson, Auckland, and Wellington will be incorporated into an incremental update in the near future.

The code repository for this work is available on GitHub ([Foster 2018](#)).

## ACKNOWLEDGMENTS

The authors are grateful to the University of Canterbury's QuakeCoRE ground motion simulation computational team for helpful advice and support, especially Daniel Lagrava, Sung Bae, and Viktor Polak. We appreciate useful feedback from Seokho Jeong, Alan Yong, David Wald, Sean Ahdi, Chris Wills, Bruce Worden, Eric Thompson, and three anonymous reviewers. This work was supported by a Marsden Fund research grant and by QuakeCoRE, a New Zealand Tertiary Education Commission-funded Centre. This is QuakeCoRE Publication Number 0346.

## ONLINE SUPPLEMENT

Please refer to the online version of this manuscript to access the supplementary material.

## REFERENCES

- Ahdi, S. K., Stewart, J. P., Ancheta, T. D., Kwak, D. Y., and Mitra, D., 2017a. Development of VS profile database and proxy-based models for VS30 prediction in the Pacific Northwest region of North America, *Bulletin of the Seismological Society of America* **107**, 1781–1801.
- Ahdi, S. K., Stewart, J. P., Kwak, D. Y., Ancheta, T. D., and Mitra, D., 2017b. Proxy-based  $V_{S30}$  prediction in Alaska accounting for limited regional data, Paper No. 482, in *Proceedings, Third International Conference on Performance-Based Design in Earthquake Geotechnical Engineering*, 16–19 July, 2017, Vancouver, Canada.
- Allen, T. I., and Wald, D. J., 2007. *Topographic Slope as a Proxy for Seismic Site-Conditions ( $V_{S30}$ ) and Amplification Around the Globe*, Open-File Report 2007-1357, U.S. Geological Survey, Reston, VA.
- Barringer, J. R. F., Pairman, D., and McNeill, S. J., 2002. *Development of a High-Resolution Digital Elevation Model for New Zealand*, Landcare Research Contract Report LC0102/170, Landcare Research, Lincoln, New Zealand.

- Borcherdt, R. D., 1994. Estimates of site-dependent response spectra for design (methodology and justification), *Earthquake Spectra* **10**, 617–653.
- Cousins, W. J., Perrin, N. D., McVerry, G. H., Hefford, R. T., and Porritt, T. E., 1996. *Ground Conditions at Strong-Motion Recording Sites in New Zealand, Report 96/33*, Institute of Geological & Nuclear Sciences, Lower Hutt, New Zealand.
- Cox, B. R., Wood, C. M., Deschenes, R., and Pearson, M., 2011. *University of Arkansas Preliminary Data Report for: Surface Wave Testing in Christchurch, New Zealand Affected by the New Zealand Earthquakes, Work Performed in Conjunction with the NSF RAPID Proposal: Liquefaction and Its Effects on Buildings and Lifelines in the February 22, 2011 Christchurch, New Zealand Earthquake*, University of Arkansas, Fayetteville.
- Cox, B. R., Wood, C. M., and Teague, D. P., 2014. Synthesis of the UTexas1 surface wave dataset blind-analysis study: Inter-analyst dispersion and shear wave velocity uncertainty, in *Geo-Congress 2014 Technical Papers: Geo-Characterization and Modeling for Sustainability (GSP 234)*, American Society of Civil Engineers, Reston, VA, 850–859.
- D'Agostini, G., 2003. *Bayesian Reasoning in Data Analysis: A Critical Introduction*, World Scientific, Singapore, 352 pp.
- Deschenes, M. R., Wood, C. M., Wotherspoon, L. M., Bradley, B. A., and Thomson, E., 2018. Development of deep shear wave velocity profiles in the Canterbury Plains, New Zealand, *Earthquake Spectra* **34**, 1065–1089.
- Destegul, U., Dellow, G., and Heron, D., 2009. A ground shaking amplification map for New Zealand, *Bulletin of the New Zealand Society for Earthquake Engineering* **42**, 122.
- Diggle, P. J., and Ribeiro, P. J., Jr, 2007. *Model-Based Geostatistics*, Springer, New York, NY, 232 pp.
- Farr, T. G., Rosen, P. A., Caro, E., Crippen, R., Duren, R., Hensley, S., Kobrick, M., Paller, M., Rodriguez, E., Roth, L., Seal, D., Shaffer, S., Shimada, J., Umland, J., Werner, M., Oskin, M., Burbank, D., and Alsdorf, D., 2007. The Shuttle Radar Topography Mission, *Reviews of Geophysics* **45**, RG2004.
- Foster, K., 2018. Vs30 model for New Zealand based on geology, terrain and observational data inputs, available at [https://github.com/fostergeotech/Vs30\\_NZ](https://github.com/fostergeotech/Vs30_NZ) (last accessed July 2019).
- Gelman, A., Carlin, J. B., Stern, H. S., Dunson, D. B., Vehtari, A., and Rubin, D. B., 2014. *Bayesian Data Analysis*, 3rd edition, CRC Press, Boca Raton, FL, 639 pp.
- GNS Science, 2016. *1:250000 Geological Map of New Zealand (QMAP)*, available at <https://www.gns.cri.nz/Home/Our-Science/Land-and-Marine-Geoscience/Regional-Geology/Geological-Maps/1-250-000-Geological-Map-of-New-Zealand-QMAP> (last accessed August 2019).
- Horn, B. K. P., 1981. Hill shading and the reflectance map, *Proceedings of the IEEE* **69**, 14–47.
- Iwahashi, J., and Pike, R. J., 2007. Automated classifications of topography from DEMs by an unsupervised nested-means algorithm and a three-part geometric signature, *Geomorphology* **86**, 409–440.
- Jayaram, N., and Baker, J. W., 2009. Correlation model for spatially distributed ground-motion intensities, *Earthquake Engineering and Structural Dynamics* **38**, 1687–1708.
- Kaiser, A., Van Houtte, C., Perrin, N., Wotherspoon, L., and McVerry, G., 2017. Site characterisation of GeoNet stations for the New Zealand strong motion database, *Bulletin of the New Zealand Society for Earthquake Engineering* **50**, 39–49.
- Kwok, O. L. A., Stewart, J. P., Kwak, D. Y., and Sun, P. -L., 2018. Taiwan-specific model for V<sub>S30</sub> prediction considering between-proxy correlations, *Earthquake Spectra* **34**, 1973–1993.

- Landcare Research New Zealand, 2010. New Zealand Digital Elevation Model 25-Metre, available at <https://iris.scinfo.org.nz/data/category/elevation/> (last accessed August 2019).
- Lee, C. -T., and Tsai, B. -R., 2008. Mapping Vs30 in Taiwan, *Terrestrial, Atmospheric and Oceanic Sciences* **19**, 671–682.
- McElreath, R., 2015. *Statistical Rethinking: A Bayesian Course with Examples in R and Stan*, CRC Press, Boca Raton, FL, 469 pp.
- McGann, C. R., Bradley, B. A., and Cubrinovski, M., 2017. Development of regional  $V_{S30}$  Model and typical  $V_s$  profiles for Christchurch, New Zealand from CPT data and region-specific CPT- $V_s$  correlation, *Soil Dynamics and Earthquake Engineering* **95**, 48–60.
- McGann, C. R., Bradley, B. A., Taylor, M. L., Wotherspoon, L. M., and Cubrinovski, M., 2015. Development of an empirical correlation for predicting shear wave velocity of Christchurch soils from cone penetration test data. *Soil Dynamics and Earthquake Engineering* **75**, 66–75.
- Moss, R. E. S., 2008. Quantifying measurement uncertainty of thirty-meter shear-wave velocity, *Bulletin of the Seismological Society of America* **98**, 1399–1411.
- Parker, G. A., Harmon, J. A., Stewart, J. P., Hashash, Y. M. A., Kottke, A. R., Rathje, E. M., Silva, W. J., and Campbell, K. W., 2017. Proxy-based VS30 estimation in Central and Eastern North America, *Bulletin of the Seismological Society of America* **107**, 117–131.
- Pebesma, E. J., 2014. *Gstat User's Manual (Version 2.5.1)*, Free Software Foundation, Boston, MA, available at <http://gstat.org/gstat.pdf>(last accessed August 2019).
- Perrin, N. D., Heron, D., Kaiser, A., and Van Houtte, C., 2015.  $V_{S30}$  and NZS 1170.5 site class maps of New Zealand, in *Proceedings, 2015 NZSEE Conference*, New Zealand Society for Earthquake Engineering, Wellington, New Zealand, 10–12.
- Standards New Zealand, 1992. *Code of Practice for General Structural Design and Design Loadings for Buildings, NZS 4203:1992*, Wellington, New Zealand.
- Standards New Zealand, 2004. *Structural Design Actions: Part 5: Earthquake Actions – New Zealand, NZS 1170.5:2004*, Wellington, New Zealand.
- Teague, D., Cox, B., Bradley, B., and Wotherspoon, L., 2018. Development of deep shear wave velocity profiles with estimates of uncertainty in the complex interbedded geology of Christchurch, New Zealand, *Earthquake Spectra* **34**, 639–672.
- Thompson, E. M., and Wald, D. J., 2012. Developing Vs30 site-condition maps by combining observations with geologic and topographic constraints, in *Proceedings, 15th World Conference on Earthquake Engineering*, 24–28 September, 2012, Lisbon, Portugal.
- Thompson, E. M., Wald, D. J., and Worden, C. B., 2014. A Vs30 map for California with geologic and topographic constraints, *Bulletin of the Seismological Society of America* **104**, 2313–2321.
- Van Houtte, C., Ktenidou, O. -J., Larkin, T., and Holden, C., 2014. Hard-site  $\kappa_0$  (kappa) calculations for Christchurch, New Zealand, and comparison with local ground-motion prediction models, *Bulletin of the Seismological Society of America* **104**, 1899–1913.
- Vilanova, S. P., Narciso, J., Carvalho, J. P., Lopes, I., Quinta-Ferreira, M., Pinto, C. C., Moura, R., Borges, J., and Nemser, E. S., 2018. Developing a geologically based VS30 site-condition model for Portugal: Methodology and assessment of the performance of proxies, *Bulletin of the Seismological Society of America* **108**, 322–337.
- Wald, D. J., McWhirter, L., Thompson, E., and Hering, A. S., 2011. A new strategy for developing VS30 maps, in *Proceedings, 4th IASPEI/IAEE International Symposium: Effects of Surface Geology on Seismic Motion*, 23–26 August, 2011, Santa Barbara, CA.



- Wills, C. J., and Clahan, K. B., 2006. Developing a map of geologically defined site-condition categories for California, *Bulletin of the Seismological Society of America* **96**, 1483–1501.
- Wills, C., and Gutierrez, C., 2009. Investigation of geographic rules for improving site-conditions mapping, in *Digital Mapping Techniques '08—Workshop Proceedings, U.S. Geological Survey Open-File Report 2009-1298*, U.S. Geological Survey, Reston, VA, 205–216.
- Wood, C. M., Cox, B. R., Green, R. A., Wotherspoon, L. M., Bradley, B. A., and Cubrinovski, M., 2017. Vs-based evaluation of select liquefaction case histories from the 2010-2011 Canterbury earthquake sequence, *Journal of Geotechnical and Geoenvironmental Engineering* **143**, 04017066.
- Wood, C. M., Cox, B. R., Wotherspoon, L. M., and Green, R. A., 2011. Dynamic site characterization of Christchurch strong motion stations, *Bulletin of the New Zealand Society for Earthquake Engineering* **44**, 195–204.
- Worden, C. B., Thompson, E. M., Baker, J. W., Bradley, B. A., Luco, N., and Wald, D. J., 2018. Spatial and spectral interpolation of ground-motion intensity measure observations, *Bulletin of the Seismological Society of America* **108**, 866–875.
- Wotherspoon, L., Bradley, B., Thompson, E., Wood, C., Deschenes, M., and Cox, B., 2016. *Dynamic Site Characterisation of Canterbury Strong Motion Stations Using Active and Passive Surface Wave Testing: Version 1.0 – June 2016*, Earthquake Commission Report Project No. 14/663, University of Auckland, New Zealand.
- Wotherspoon, L., Orense, R., Bradley, B., Cox, B., Wood, C., and Green, R., 2013. *Geotechnical Characterization of Christchurch Strong Motion Stations: Version 1.0 – September 2013*, Earthquake Commission Report Project No. 12/629, University of Auckland, New Zealand.
- Yong, A., 2016. Comparison of measured and proxy-based  $V_{S30}$  values in California, *Earthquake Spectra* **32**, 171–192.
- Yong, A., Hough, S. E., Iwahashi, J., and Braverman, A., 2012. A terrain-based site-conditions map of California with implications for the contiguous United States, *Bulletin of the Seismological Society of America* **102**, 114–128.

(Received 11 December 2018; Accepted 6 May 2019)